# Low Frequency Climate Response of Quasigeostrophic Wind-Driven Ocean Circulation

Rafail V. Abramov *

*Department of Mathematics, Statistics and Computer Science*

*University of Illinois at Chicago*

*Chicago, Illinois, U.S.A.*

Andrew J. Majda

*Department of Mathematics and Center for Atmosphere Ocean Science*

*Courant Institute of Mathematical Sciences, New York University*

*New York City, New York, U.S.A.*

* *Corresponding author address:* Rafail Abramov, Department of Mathematics, Statistics and Computer Science, University of Illinois at Chicago, 851 S. Morgan St., Chicago, IL 60607.

E-mail: abramov@math.uic.edu

ABSTRACT

Linear response to external perturbation through the fluctuation-dissipation theorem has recently become a popular topic in the climate research community. It relates an external perturbation of climate dynamics to climate change in a simple linear fashion, which provides key insight into physics of the climate change phenomenon. Recently, the authors developed a suite of linear response algorithms for low frequency response of large scale climate dynamics to external perturbation, including the novel blended response algorithm which combines the geometrically exact general response formula using integration of a linear tangent model at short response times, and the classical quasi-Gaussian response algorithm at longer response times, overcoming numerical instability of the tangent linear model for longer times due to positive Lyapunov exponents. Here we apply the linear response framework to several leading empirical orthogonal functions of a quasigeostrophic model of wind-driven ocean circulation. It is demonstrated that the actual nonlinear response of this system under external perturbation at leading EOFs can be predicted by the linear response algorithms with adequate skill with moderate errors; in particular, the blended response algorithm has a pattern correlation with the ideal response operator on the four leading EOFs of the mean state response of 94% after 5 years. In addition, remarkable physical properties of the mean flow response to large scale changes in wind stress at the leading EOFs are observed.

# 1. Introduction

The low frequency response to external perturbations for various components of the climate system is a central problem of contemporary climate change science. In particular,

in the ocean, it is vital to understand the feedback of large scale ocean currents (such as the Gulf Stream or Kuroshio) to changes in the mean external wind forcing, which by itself could be caused by climate changes in the lower troposphere. In this work, the authors use the linear response algorithms, based on the fluctuation-dissipation theorem (FDT), to predict the response of a prototype model of the Gulf Stream and Kuroshio currents (McCalpin (1995); McCalpin and Haidvogel (1996)) to external perturbations at leading large scale empirical orthogonal functions (EOF).

Despite the fact that the climate system is a complex chaotic multiscale problem with forcing, dissipation, and the equilibrium state structure has significant complexity, there has been a profound interest among the atmospheric/ocean science community to apply the fluctuation-dissipation theorem to predict global climate changes responding to variation of certain physical parameters. Leith (1975) suggested the possibility that, despite the absence of the classical Gaussian equilibrium state, the fluctuation-dissipation theorem might constitute a sensible approximation for appropriate variables in the complex climate system, and a way to predict climate change by utilizing suitable statistics of the present climate. Leith's approximation has been called the quasi-Gaussian (qG-FDT) approximation in Majda et al. (2005), where it is studied theoretically and computationally. Leith's suggestion has inspired others such as Bell (1980), Carnevale et al. (1991), Gritsun (2001), Gritsun et al. (2002), Gritsun and Dymnikov (1999) to apply the quasi-Gaussian fluctuation-dissipation theorem for idealized climate models with various approximations and numerical procedures. Gritsun and Branstator (2007), and Gritsun et al. (2008) for computing the response of the mean state and variance, respectively, have applied the quasi-Gaussian approximation to a comprehensive general circulation model with interesting results.

In the past several years, the authors developed a suite of practical linear response algorithms beyond the standard classical quasi-Gaussian FDT approximation. Abramov and Majda (2007, 2008, 2009) developed the short-time FDT (ST-FDT) response algorithm (itself based on theory in Ruelle (1998)) for deterministic chaotic dynamical systems with singular invariant statistical states (SRB measures), which is inherently numerically unstable due to positive Lyapunov exponents, and the blended ST/qG-FDT algorithm which combines the ST-FDT algorithm at shorter response times for better precision, and qG-FDT algorithm at longer response times to improve numerical stability. Abramov (2009, 2010, 2011) made further improvements to the new algorithm, adapting it for use with a reduced-rank tangent linear model to reduce computational expense, for slow-fast multiscale dynamics (as Majda et al. (2010b) did for classical FDT), and for stochastically driven dynamics. Majda et al. (2010a) explored the issue of structural instability of singular statistical states under external forcing and predictive skill despite irreducible imprecision. Majda and Wang (2010), and Gershgorin and Majda (2010) extended the linear response framework for use with time-dependent periodically forced dynamical systems. Majda and Hairer (2010) provided a rigorous justification for linear response theory.

The current work is organized as follows. Section 2 describes the prototype model for the Gulf Stream-like large scale eastward ocean flow, developed by McCalpin (1995) and McCalpin and Haidvogel (1996), as well as its technical implementation and numerical simulation parameters. In Section 3 we present the numerical simulation results of the low-frequency climatology of the model's large scale empricial orthogonal functions and their physical interpretation, as well as the global Lyapunov exponents of the model together with mixing properties. Section 4 describes the linear response algorithms used to predict

the response of the flow. In Section 5 we present the numerical simulation results of the prototype model response to external perturbation at leading EOFs. In Section 6 we study the patterns of perturbations which cause response with largest magnitude at prescribed time. Section 7 summarizes the results of this work.

## 2. The prototype model of the wind driven ocean circulation

The 1.5 layer quasigeostrophic double gyre model, described by McCalpin (1995), McCalpin and Haidvogel (1996), is given by

$$\begin{aligned}(\Delta - \gamma^2)\frac{\partial h}{\partial t} = -\frac{g'}{f_0}\nabla^{\perp}h \cdot \nabla(\Delta h) - \beta\frac{\partial h}{\partial x} - \\ - r\Delta h - A_b\Delta^3 h + \frac{f_0}{\rho_0 g' H}\mathrm{curl}\,\vec{\tau},\end{aligned} \tag{1}$$

where $\nabla$ is the gradient operator, $\Delta = \nabla^2$ is the Laplace operator, $h$ is the interface anomaly (positive upward), $r$ is the coefficient of interfacial friction, $A_b$ is the coefficient of higher-order viscosity (hyperviscosity), $\tau$ is the wind stress on the ocean surface, $\rho_0$ is the mean density of seawater, $H$ is the reference thickness of the upper layer, $f_0$ is the Coriolis parameter in the middle of the domain, and $\beta$ is the latitudinal derivative of the Coriolis parameter in the middle of the domain. In the current set-up, these parameters are set to the same values as in McCalpin and Haidvogel (1996), and are shown in Table 1. The choice of $f_0$ and $\beta$ parameters corresponds to the 30° latitude in the Northern Hemisphere. The parameter $\mathrm{curl}\,\vec{\tau}$ is chosen to simulate a slightly asymmetric wind stress

$$\mathrm{curl}\,\vec{\tau} = \tau_0\frac{2\pi}{L_y}\sin\left(\frac{2\pi y}{L_y}\right)\left[1 - 4\alpha\left(\frac{y}{L_y} - \frac{1}{2}\right)\right], \tag{2}$$

where $0 \leq y \leq L_y$ is the meridional distance from the southern boundary of the domain. The value of $\tau_0$ in (2) is set to $0.05\,N\,m^{-2}$. The parameter $\alpha$ in (2) governs the asymmetry of the wind stress, and is set to 0.05 which ensures the difference in about 10% of the peak wind stress between the northern and southern parts of the domain.

The model is solved in a rectangular domain of $L_x \times L_y = 3600 \times 2700$ km using the uniform 56.25-km grid, which results in 64 discretization points in the longitudinal direction and 48 discretization points in the latitudinal direction, constituting 3072 discretization points in total. The standard pseudospectral method (derivatives are computed in spectral space, nonlinearities in physical space) via the half-domain Discrete Sine Transform is used to compute the right-hand side of (1), which automatically satisfies the free-slip boundary condition for the flow. The standard 4th-order Runge-Kutta method with the time step of 12 hours is used to compute the time series of the solution. The initial period of $T_0 = 100$ years is skipped between the beginning of time series computation and the beginning of statistical computation to ensure that the dynamical system has settled onto its statistical steady state. Then the statistical information is computed for the $T_{av} = 10000$ years time averaging window, with the data output interval of 10 days.

# 3. Long term climatological properties of the prototype model

In this section we present long-term mean state, its variance, the empirical orthogonal functions (EOFs), as well as their statistical properties.

*a. The climatological mean state and variance*

The climatological mean state and variance are computed according to the formulas

$$\overline{h}(x,y) = \frac{1}{T_{av}} \int_{T_0}^{T_0+T_{av}} h(x,y,t)\mathrm{d}t, \tag{3a}$$

$$\mathrm{Var}\left[h\right](x,y) = \frac{1}{T_{av}} \int_{T_0}^{T_0+T_{av}} \left(h(x,y,t) - \overline{h}(x,y)\right)^2 \mathrm{d}t, \tag{3b}$$

where $T_0 = 100$ years, and $T_{av} = 10000$ years. In Figure 1 (top row) we show the 10000-year mean state and variance for the solution of (1). For the mean state, we can observe a jet, which separates from the western boundary of the rectangular basin due to the wind forcing, and has the length of approximately 1500 km. For the variance, we can observe that the variance of the solution is largely confined to the area approximately $2000 \times 1500$ km around the mean jet flow. There is a very good correspondence of the mean state with the one presented in McCalpin and Haidvogel (1996) despite substantial differences in numerical scheme implementation, and spatial and time step discretization.

*b. Empirical orthogonal functions and their principal components*

In this section we present the patterns of the four leading empirical orthogonal functions (EOFs), together with EOF eigenvalues. The EOFs are computed as eigenvectors of the covariance matrix for the Fourier modes $\hat{h}_k$ of the streamfunction according to the formula

$$\mathrm{Cov}\left[h\right]\vec{E}_k = \lambda_k \vec{E}_k, \tag{4}$$

with the covariance matrix computed as

$$\mathrm{Cov}\left[h\right]_{ij} = \frac{1}{T_{av}} \int_{T_0}^{T_0+T_{av}} \left(h_i(t) - \overline{h}_i\right)\left(h_j(t) - \overline{h}_j\right) \mathrm{d}t, \tag{5}$$

where $h_i(t)$ and $\overline{h}_i$ are the interface anomaly and its mean state, respectively, at the $i$-th discretization point in the $xy$-domain (3072 in total). The EOFs $\vec{E}_k$ are the eigenvectors of the symmetric positive definite covariance matrix in (5) and therefore are orthogonal to each other. For convenience, the EOFs are normalized in such a way that

$$\vec{E}_k \cdot \vec{E}_k = \lambda_k. \tag{6}$$

As follows from their definition, the EOFs are solution patterns which in the long run are simultaneously statistically independent, in the sense that their two-point single-time cross-correlations are identically zero. In other words, the EOFs are large-scale chunks of the flow which constitute roughly independent components of the complete flow motion in the long term. On average, each EOF contributes to the solution according to the magnitude of its corresponding eigenvalue, and thus the EOFs with largest eigenvalues (called leading EOFs) are generally more important than EOFs with smaller eigenvalues. The EOFs are ordered by their eigenvalues in descending order (such that EOF 1 has the largest eigenvalue, EOF 2 has the second largest eigenvalue, etc). The projection coefficients of EOFs onto the solution are called principal components (PCs). As follows from (6), the mean state of the long-term time series of any PC is always zero, and the PC covariance matrix is the identity matrix. Once the EOFs and PCs are found, the solution itself can be reconstructed through the formula

$$h(x,y,t) = \overline{h}(x,y) + \sum_i \mathrm{PC}_i(t)\mathrm{EOF}_i(x,y). \tag{7}$$

In Figure 1 (bottom row) we display the EOF eigenvalues in both standard and logarithmic scale. The spectrum of eigenvalues starts with the first eigenvalue of about 35, and declines slightly faster than a power law.

In Figure 2 we display the physical patterns of the leading EOFs 1–4. EOF 1 consists of one strong hoziontally elongated gyre attached to the western boundary in the middle of the meridional range of the basin, and two weaker gyres above and below this strong gyre with similar spatial structure. The size of the strong gyre is approximately $2000 \times 500$ km. According to the EOF 1 configuration, its primary function appears to shift the mean jet northward and southward, depending on the sign of the corresponding first principal component (PC1). EOF 2 consists of two strong gyres at the equator of the basin with centers approximately 500 km (left gyre) and 1000 km (right gyre) east of the western basin boundary. The size of the right, stronger, gyre is approximately $800 \times 500$ km, whereas the size of the left, weaker, gyre is approximately $600 \times 500$ km. According to the EOF 2 configuration, its primary function is to twist the straight mean flow jet into a meandering flow. EOF 3 consists mainly of the jet similar in placement to the one in the mean state, which is attached to the western boundary in the middle of the meridional range of the basin. The length of the jet in the EOF 3 is approximately 1500 km. According to the EOF 3 configuration, its primary function is to either amplify or to suppress the mean jet, depending on the sign of the corresponding principal component. EOF 3 might play a role in the intermittent behavior of the solution, when the mean jet is meandering or broken into strong gyres with short lifespan (by EOF 2). EOF 4 consists mainly of a strong $600 \times 400$ km gyre at the equator of the basin. Together with EOF 2, EOF 4 appears to constitute a mechanism of breaking the mean jet into meanders and small gyres.

*c. Statistical distribution and time correlation functions of the principal components*

By construction, the long-term time averages of principal components have zero mean state and unit variance. However, the long-term statistical distribution of PCs in this case is determined by higher-order moments. In particular, in the case of the Gaussian distribution with zero mean state and unit variance, the third moment (skeweness) is zero, and fourth moment (flatness) equals 3. By monitoring the skeweness and flatness of the PCs, one can detect deviations from Gaussianity. Here we display the skewness (third moment), flatness (fourth moment), probability density functions and time correlation functions of the principal components (PC). In Figure 3 (top row) we show the skewness and flatness of the 20 leading PCs. Observe that the non-zero skewness is concentrated at the PC of the 3rd EOF, while the rest of PCs display little skewness. As for the flatness, the PCs are clearly sub-Gaussian at large scales, and become more Gaussian at smaller scales. In Figure 5 we show the probability density functions (PDFs) for the PCs 1–4. The figures confirm the moments indications – namely, the PDF of the PC for EOF 3 is very skewed to the left. The rest of the PDFs display some skewness, but not much. In Figure 3 (bottom-left) we show the autocorrelation times (the integral of the time autocorrelation function) for the 20 leading PCs, and in Figure 4 we show the time autocorrelation functions for the four leading PCs. Observe that the autocorrelation time is largest for the first PC (around 800 days) and then decreases monotonically to about 150 days. The plots of individual autocorrelation functions confirm this trend.

*d. Lyapunov exponents*

Here in Figure 3 (bottom-right) we display the first 100 Lyapunov exponents. Observe that the first Lyapunov exponent $\lambda_1 = 5.3 \cdot 10^{-3}$, which corresponds to roughly half-year Lyapunov characteristic time. Also, there are 12 positive Lyapunov exponents. According to these results, the model can be viewed as rather weakly chaotic, however, there is no spectral gap in the Lyapunov exponents, as the spectrum decays rather smoothly.

# 4. Linear response algorithms

Here we proceed under the general assumption that the low frequency wind driven prototype model in (1) is numerically represented as a chaotic nonlinear dynamical system of ordinary differential equations for the state vector $\vec{x} \in \mathbb{R}^N$ (where for our set-up $N = 3072$), given by

$$\frac{\mathrm{d}\vec{x}}{\mathrm{d}t} = \vec{f}(\vec{x}), \tag{8}$$

where $\vec{x}$ in our case is a vector of principal components (PC) corresponding to the model EOFs. Let $A(\vec{x})$ be a linear or nonlinear response function which is a part of the model climatology (in the mean flow response tests below, $A(\vec{x})$ is set to represent the response of the flow mean state or its variance). The average value $\langle A \rangle$ of $A(\vec{x})$ for the dynamics in (8) is computed as a time average along a single long-term trajectory of (8):

$$\langle A \rangle = \frac{1}{T_{av}} \int_{T_0}^{T_0+T_{av}} A(\vec{x}(t))\mathrm{d}t. \tag{9}$$

We assume that the dynamical system in (8) is perturbed by a small external forcing as

$$\frac{\mathrm{d}\vec{y}}{\mathrm{d}t} = \vec{f}(\vec{y}) + \delta\vec{f}, \tag{10}$$

where for our set-up we assume that $\delta\vec{f}$ is constant, although in general it can depend on both $\vec{x}$ and $t$ (for details, see, for example, Abramov and Majda (2007, 2008, 2009)). In our framework, the external forcing represents the collection of altered geophysical parameters, such as the change in wind stress due to altered atmospheric climatology. Apparently, the solution $\vec{y}(t)$ will cause $\langle A\rangle$ to deviate from its original value, which represents the climate response to change in the external parameters:

$$\delta\langle A\rangle = \frac{1}{T_{av}}\int_{T_0}^{T_0+T_{av}} [A(\vec{y}(t)) - A(\vec{x}(t))]\mathrm{d}t. \tag{11}$$

The formula in (11) provides a straightforward estimate for the response of the model climatology, based on the distance between two different numerically simulated long-term trajectories of the perturbed and unperturbed models, respectively. However, it requires separate long-term numerical simulation with the prototype model in (1) for each perturbation, which can be prohibitively numerically expensive in the case of multiple perturbations (corresponding to different atmospheric climate change scenarios). Also, it computes the response at long time, and provides no information about transient time-dependent behavior of response of the model climatology when the changes in external forcing are applied to the dynamics.

Provided that the change in external forcing is small, the fluctuation-dissipation theorem (FDT) offers a more versatile way to construct an approximation for $\delta\langle A\rangle$:

$$\delta\langle A\rangle(t) = \vec{R}(t)\cdot\delta\vec{f}, \tag{12}$$

where $t = 0$ is the initial time when the forcing change is introduced into the dynamical system. Here $\vec{R}(t)$ is the *linear response operator*, which directly relates the changes in

external parameters $\delta\vec{f}$ to the climate response $\delta\langle A\rangle$. Note that $\vec{R}(t)$ does not depend on the magnitude and direction of $\delta\vec{f}$, and, once computed, provides the climate response for a wide range of magnitudes and directions $\delta\vec{f}$. Also one can study $\vec{R}(t)$ directly to determine which changes in $\delta\vec{f}$ will result in a most catastrophic (or otherwise, most insignificant) response of $\delta\langle A\rangle$ (Majda et al. (2005); Gritsun et al. (2008)). Additionally, the formula in (12) provides the time-dependent climate response for finite values of $t$, which allows the study of transient climate change effects. Below we describe several methods to compute the linear response operator in (12). Note that $\vec{R}(t)$ is a vector for a scalar response function $A(\vec{x})$; if the response function is by itself vector-valued, then the response operator will consist of a set of vectors (one for each component of $\vec{A}(\vec{x})$), that is, the response operator will be a matrix.

*a. Quasi-Gaussian FDT (qG-FDT) method*

Under the assumption of nearly Gaussian probability distribution for the long-term climatological equilibrium, and given the fact that $\vec{x}$ is a vector of principal components of the EOFs, the response operator $\vec{R}(t)$ is evaluated as the integral of the time autocorrelation function (Deker and Haake (1975); Majda et al. (2005); Abramov and Majda (2007, 2008, 2009); Gritsun et al. (2008); Risken (1988))

$$\vec{R}_{qG}(t) = \frac{1}{T_{av}} \int_{T_0}^{T_0+T_{av}} \int_0^t A(\vec{x}(\tau+s))\vec{x}(s)\mathrm{d}\tau\mathrm{d}s. \tag{13}$$

The formula in (13) is the quasi-Gaussian FDT (qG-FDT) response operator. The response formula in (13) with $A(\vec{x}) = \vec{x}$ was originally suggested by Leith (1975).

The main advantage of the quasi-Gaussian formula in (13) is its relative simplicity and

low computational cost for a simple response function $A(\vec{x})$, such as the response of the mean state of a PC or its variance. However, it is efficient only for dynamical regimes with nearly Gaussian equilibrium state and robust mixing dynamics, see Majda et al. (2005) and Abramov and Majda (2007, 2008, 2009). For a strongly non-Gaussian climatology with slow decay of correlation functions, the qG-FDT response algorithm rapidly loses its precision.

*b. Short-time FDT (ST-FDT) method*

A wide variety of practical geophysical models are complex nonlinear chaotic forced-dissipative dynamical systems with statistical attractors which are not smooth. The equilibrium states on such attractors are typically Sinai-Ruelle-Bowen (SRB) probability measures (for details see Eckmann and Ruelle (1985), Ruelle (1997, 1998) and Young (2002)). Abramov and Majda (2007, 2008, 2009) reworked the FDT formula in such a way that an approximation to the equilibrium state is not required to compute the response, thus adapting the response formula to an arbitrary equilibrium state. This method is exact for a general dynamical system and is called short-time FDT (ST-FDT), due to its inherent numerical instability at longer times for chaotic dynamical systems. With this method, the time autocorrelation function is given by

$$\vec{R}_{ST}(t) = \frac{1}{T_{av}} \int_{T_0}^{T_0+T_{av}} \int_0^t \nabla A\left(\vec{x}(\tau+s)\right) \boldsymbol{T}^{\tau}_{\vec{x}(s)} \mathrm{d}\tau \mathrm{d}s, \tag{14}$$

where $\boldsymbol{T}^t_{\vec{x}}$ is a tangent map at $\vec{x}$ to $t$, which is computed as an $N \times N$ (3072 by 3072 in our case) matrix by solving the equation

$$\frac{\mathrm{d}\boldsymbol{T}}{\mathrm{d}t} = \nabla \vec{f} \boldsymbol{T}, \tag{15}$$

where $\nabla \vec{f}$ is the Jacobian of $\vec{f}$, also an $N \times N$ matrix. The ST-FDT response formula in (14) provides the precise response approximation for an arbitrary climatological equilibrium state, regardless of the dynamical robustness and mixing. The main drawback of the ST-FDT method is that the unstable Lyapunov directions of the tangent map in (15) grow exponentially in time and create numerical instability in (14) for long response times. Also, the ST-FDT method is computationally more expensive than the qG-FDT method, and, to avoid excessive computational expense, here we used the reduced-rank tanget map algorithm with rank 1536, which is half of the total dimension 3072 of the model phase space (for details on the reduced-rank tangent map algorithm, see Abramov (2009)). The detailed description of the ST-FDT method and its numerical implementation for computing (14) and (15) are given in Abramov and Majda (2007, 2008, 2009) with illustrative detailed applications.

*c. Blended ST/qG-FDT method*

In the previous two sections we observed that the ST-FDT response operator and the qG-FDT approximation have somewhat opposite advantages and drawbacks. Namely, while for shorter response times the ST-FDT approximation is superior to the qG-FDT response operator due to its precise geometric interpretation of the response formula in (14), it eventually blows up at longer times due to exponential growth in positive Lyapunov directions. On the other hand, the qG-FDT response operator is free of numerical instabilities, but produces larger errors for weakly mixing non-Gaussian regimes. However, there is a simple way to avoid the blowup and increase the overall accuracy by blending the ST-FDT response with the qG-FDT response at later times before the numerical blow-up occurs, thus combining

the best properties of both responses through the following formula:

$$\vec{R}_{ST/qG}(t) = \begin{cases} \vec{R}_{ST}(t), & t \le T_{\text{cutoff}}, \\ \dfrac{1}{T_{av}} \displaystyle\int_{T_0}^{T_0+T_{av}} \Big( \int_0^{T_{\text{cutoff}}} \nabla A\left(\vec{x}(\tau+s)\right) \boldsymbol{T}^{\tau}_{\vec{x}(s)} \mathrm{d}\tau + \\ \qquad + \displaystyle\int_{T_{\text{cutoff}}}^{t} A(\vec{x}(\tau+s))\vec{x}(s)\mathrm{d}\tau \Big) \mathrm{d}s, & t > T_{\text{cutoff}}, \end{cases} \tag{16}$$

where $T_{\text{cutoff}}$ is the cutoff time chosen just before the numerical instability occurs in $\vec{R}_{ST}$. The blended response operator $\vec{R}_{ST/qG}$ combines the advantages of the ST-FDT for shorter times, and qG-FDT for longer times. In the present work, we set the cutoff time to one year, as it is practically observed that the numerical instability in the ST-FDT response develops shortly after one year response time. Implementations of the blended response algorithm in other large-dimensional chaotic dynamical systems are found in Abramov and Majda (2007, 2009); Abramov (2011).

# 5. Linear response of the large scale PCs of the prototype model

In this section we present the results of direct numerical simulations with the prototype model in (1), where the external perturbations are applied separately at the first 4 individual model PCs, one PC at a time. For each perturbed PC, we measure the response of the two response functions (mean state and variance), also at first 4 individual PCs (which are 0 and 1, respectively, at the unperturbed state). In total, this constitutes 16 ($4 \times 4$) combinations of perturbed and responding PCs for each response function, with 32 plots in total. For each combination of perturbed and responding PC, we plot the normalized response $\delta\langle A\rangle/\delta f$,

which corresponds to an appropriate entry of the linear response operator $\vec{R}$. Together with the computed entries of linear response operators according to algorithms in Section 4, we also plot the directly measured ratio $\delta\langle A\rangle/\delta f$ for each combination of perturbed and responding EOFs, averaged over several perturbations of different magnitudes (so-called ideal response, see Abramov and Majda (2007, 2008, 2009) and references therein) to compare the actual response of the prototype model with its FDT predictions from Section 4.

Also, for each response function we show the bulk relative error and correlation functions between the $4 \times 4$ matrices of the ideal response operator and each of qG-FDT and ST/qG-FDT operators. The relative error function is given as the Frobenius norm of the difference between the ideal and either qG-FDT or ST/qG-FDT responses, normalized by the Frobenius norm of the ideal response matrix (recall that the Frobenius norm of a matrix is the square root of the sum of squares of all matrix entries). The correlation function is given by the sum of all entries of the Hadamard product of the ideal and either qG-FDT or ST/qG-FDT response matrices, normalized by the product of Frobenius norms of these response matrices. Thus, by construction, the relative error response function provides the standard quadratic normalized error norm between the actual response of the prototype model in (1) and predicted qG-FDT or ST/qG-FDT response, while the correlation function provides the error in the direction of the response regardless of difference in magnitude, since this is often of primary interest (it is not hard to see that if the qG-FDT or ST/qG-FDT response is a positive multiple of the ideal response, the correlation function will be equal to 1). This is done for separate study of the overall error and directional error, since in most applications the direction error of the response is quite important in its own respect, regardless of discrepancy in the response magnitude.

*a. Linear response of mean values of the PCs*

The linear response of the mean state for the first 4 PCs is shown in Figures 6–9. Here we can observe that the performance of qG-FDT response algorithm is generally not very precise, although in some cases it is quite good. The performance of the ST-FDT is generally better than that of the qG-FDT, with the blowup time roughly about 1 year, which is in good correspondence with 2 $\times$ Lyapunov characteristic time rule, mentioned earlier. It is interesting to see how the perturbation at a given PC results in responses across the first main PCs. The perturbation at PC1 results in the response in PC1 and PC3 – that is, the response of the mean jet follows the wind stress pattern shifting northward or southward, with additional amplification of the jet, with weak possibility of breaking into meanders. On the other hand, perturbing the wind stress in the meandering pattern (that is, forcing at PC2), results first in the meandering pattern response at EOF2 oscillating with period of roughly 2 years, but that is dominated by the response at EOF1, that is, the jet ultimately becomes more straightened and shifts northward or southward. Perturbing PC3 (wind stress amplification) results in the response mainly in the EOF3 pattern itself, that is, the jet is amplified without shifting northward or southward, perhaps with slight meandering. Perturbation at PC4 results in the similar results as for PC2 – namely, the response ultimately dominates at EOF1 pattern, with transient osciallations in meandering patterns.

Errorwise, the blended ST/qG-FDT algorithm with cut-off time 1 year is superior to qG-FDT for all response times. The main source of global error appears the part of the response operator which corresponds to both forcing and response at EOF 1 (upper-left plot in Figure 6) – while the actual observed response seems to stabilize around the value of 200

fairly quickly (around 3 years response time), but the qG-FDT and ST/qG-FDT response operators exhibit continuous growth in time for this entry. The rest of the diagonal entries of the response operators, as well as off-diagonal entries, do not seem to produce that much of an error. In Figure 14 we show the relative errors and correlations for the qG-FDT and ST/qG-FDT responses as compared to the ideal response. Observe that the ST/qG-FDT response is significantly more precise than the qG-FDT response, however, both responses are very highly correlated with the ideal response (the worst correlation among both methods is around 0.9 for the qG-FDT). As mentioned before, the main source of error appears to be the magnitude of the single diagonal entry of the response operator, which corresponds to both forcing and response at EOF 1.

*b. Linear response of variance of the PCs*

The linear response of the variance for the first 4 EOFs is shown in Figures 10–13. Here we can see that the relative precision of the response is generally worse than for the mean state response, for both the qG-FDT and ST/qG-FDT response algorithms. However, the ST/qG-FDT response algorithm is somewhat better than the pure qG-FDT response algorithm. Remarkably, the response of the variance is much smaller than the response of the mean state, which means that the large scale circuation of the prototype model in (1) tend to shift in the mean positions, without altering variability much. Of course, the simple ocean model studied here lacks baroclinic instability mechanisms, and this result might change in a more complex model. In Figure 14 we show the physical correlations for the qG-FDT and ST/qG-FDT responses as compared to the ideal response. Observe that in the beginning

the correlation is quite bad for both the qG-FDT and ST/qG-FDT responses, due to the fact that the magnitude of the response for short times is typically small, which amplifies all relative quantities, such as the correlation. However, at later times the correlation improves, saturating at around 60% (for qG-FDT) and 70% (for ST/qG-FDT). After one year, the correlation for the blended ST/qG-FDT response algorithm is around 0.93; however, the bad correlation at even earlier time is due to the tiny response magnitude of the variance.

# 6. Perturbations with largest response magnitude at prescribed response time

When studying the average response to small, but constant perturbation, the problem of attribution of perturbation direction to the response with a given property at a prescribed time is of great importance (Majda et al. (2005); Gritsun et al. (2008)). In particular, a key question is what perturbation causes response with the largest magnitude at a prescribed response time. If the response function is scalar, then from the FDT linear relation in (12) it follows that the perturbation $\delta\vec{f}$ with largest response magnitude should be collinear to the vector linear response operator $\vec{R}(t)$. However, when the response function is a vector, the FDT framework relates the vector of perturbation to the vector of response through the matrix linear response operator $\boldsymbol{R}(t)$:

$$\delta\langle\vec{A}\rangle(t) = \boldsymbol{R}(t) \cdot \delta\vec{f}. \tag{17}$$

In our situation, the response function is a vector – either 4-dimensional vector of EOF mean states, or their variances. Thus, the linear response operator $\boldsymbol{R}(t)$ is a $4 \times 4$ time-dependent

matrix. In this case one can use the singular value decomposition (SVD) to determine the perturbation which provides response with largest magnitude:

$$\boldsymbol{R}(t) = \boldsymbol{U}\boldsymbol{S}\boldsymbol{V}^T, \tag{18}$$

where $\boldsymbol{S}$ is the diagonal matrix of singular values, and columns of $\boldsymbol{U}$ and $\boldsymbol{V}$ constitute the left and right singular vectors, respectively. Here, the direction of the response with largest magnitude is the column of $\boldsymbol{U}$ which corresponds to the largest singular value in $\boldsymbol{S}$, and the direction of perturbation which causes largest magnitude response is the corresponding column of $\boldsymbol{V}$. Then, these singular perturbation and response directions can be projected onto the corresponding combination of the EOF patterns in physical space.

In Figures 15–17 we display the singular perturbation and response patterns corresponding to 1, 2 and 5 year response time of the mean state. Observe that the singular perturbation for 1-year response consists mainly of the EOF 1, with smaller contributions from EOFs 3 and 4, while the corresponding singular response mainly appears at the EOF 3, which generally means that imposing vertical shift of wind shear for one year mainly affects the strength of the mean jet. For 2 and 5 year response, both the singular perturbation and response are mainly shared between EOFs 1 and 3, connecting vertical shifts of both wind pattern and mean jet to its strength. It is interesting that EOFs 2 and 4 (which are responsible for breaking the mean jet and creation of vortices) do not play a key role in singular perturbation-response teleconnections. Also observe that the correlation of the ST/qG-FDT singular perturbation-response patterns with the ideal patterns is much better than those predicted by the qG-FDT method.

In Figures 18–20 we display the singular perturbation and response patterns correspond-

ing to 1, 2 and 5 year response time of the variance. This type of response is remarkably interesting from the physical perspective, since it connects mean perturbation pattern with changes in variability (and thus uncertainty) patterns, rather than its mean state response. Here we found that the singular value spectrum for the blended ST/qG-FDT linear response operator has a narrow gap between the first and second singular values, and due to numerical errors incorrect ordering of singular values by magnitude results for the blended ST/qG-FDT algorithm. Thus, in what follows the set of singular vectors corresponding to the second largest singular value of the ST/qG-FDT response operator is treated as the singular perturbation-response direction. Here the directly measured ideal response singular perturbation-response patterns mainly appear at EOFs 3 and 1 (for singular perturbations) and EOFs 2 and 4 (for singular responses). The blended ST/qG-FDT response operator produces the prediction close to what is directly measured, while the corresponding qG-FDT predictions indicate singular perturbations and response mainly concentrated at EOF 1 and EOF 3, respectively. From the physical viewpoint, the qG-FDT algorithm predicts the singular variance response to be along the jet-amplifying patterns, while the blended ST/qG-FDT algorithm and direct measurements show the singular variance response appearing in jet-breaking patterns.

# 7. Summary

In earlier work, the authors developed a set of practical linear response algorithms beyond the standard classical quasi-Gaussian FDT approximation. Abramov and Majda (2007, 2008, 2009) developed the short-time FDT (ST-FDT) response algorithm (itself based on

theory in Ruelle (1998)) for deterministic chaotic dynamical systems with singular invariant statistical states (SRB measures), which is inherently numerically unstable due to positive Lyapunov exponents, and the blended ST/qG-FDT algorithm which combines the ST-FDT algorithm at shorter response times for better precision, and qG-FDT algorithm at longer response times to improve numerical stability. Abramov (2009) made further improvements to the new algorithm, adapting it for use with a reduced-rank tangent linear model to reduce computational expense. The main goal of this work was to study and document the performance of the developed algorithms for the prediction of the response of large scale wind driven ocean flow to the change in an external wind forcing, as well as to observe the physical properties of the leading model EOFs and cross-response teleconnection patterns between different perturbed and response EOFs, for the 5 year response time window.

We found that the structure of the first four leading EOFs covers three basic types of the mean flow response: first, the shifting of the mean jet northward or southward (EOF 1), second, the amplification or suppression of the mean jet (EOF 3), and, third, breaking of the mean jet into meanders and gyres (EOFs 2 and 4). The following response trends were observed:

- When the wind stress pattern shifts northward or southward (EOF 1), the mean flow jet generally follows the change in the wind stress, that is, the bulk of the response is also observed at EOF 1. In addition, there is an extra response at EOF 3, which amplifies or weakens the central mean jet. No substantial response at EOFs 2 and 4 is observed in this case, which means that the mean flow jet is stable under this type of perturbation (no meandering develops).

- When the wind stress pattern is altered to amplify or weaken the mean jet (EOF 3), it results in the response mainly in the EOF 3 pattern itself, that is, the jet is amplified without shifting northward or southward, perhaps with slight meandering.

- Remarkably, perturbing the wind stress in a meandering pattern (that is, forcing at EOF 2 or 4), results first in the meandering pattern response at EOF 2 or 4, but that later in time is dominated by the response at EOF1, that is, the jet ultimately becomes more straightened and shifts northward or southward.

- The projections of singular perturbations which cause largest magnitude response of the mean state onto the first four EOFs are captured exceptionally well by the blended ST/qG-FDT method, and somewhat worse by the qG-FDT method. It is found that the singular perturbation-response patterns of the mean state are tied mainly to the EOFs 1 and 3, which are attributed to the mean jet strength and direction. Thus, jet-breaking wind patterns would not cause significant response, nor would the jet-breaking component of a flow response be significant. For the variance response and singular patterns of changed variability, the qG-FDT algorithm essentially fails to capture direct response measurements, where singular response appears chiefly in jet-breaking patterns. However, the blended ST/qG-FDT algorithm prediction is quite similar to the direct measurements. Also, the observed directional correlation between the ideal and the blended ST/qG-FDT variance response is quite good (about 93% at one year response).

The relative errors in the linear response algorithms (as compared to the ideal response) are rougly 25%/year for the qG-FDT algorithm, due to non-Gaussianity and weak mixing,

and about 5% during the first year for the ST/qG-FDT algorithm, with the same error trend as for the qG-FDT after the cut-off time. However, the correlation results are quite remarkable, namely, the maximum decorrelation at 5 year response time for the ST/qG-FDT is 94%, and 90% for the qG-FDT algorithm. Thus, one can conclude that although the overall response precision is not very impressive, the direction of the response is captured with great predictive skill. The variance at the four leading EOFs is found not to be very responsive to the wind stress perturbations at the same set of the EOFs (overall response is much smaller than that of the mean state).

*Acknowledgments.*

Both authors are jointly supported by the Office of Naval Research grant 25-74200-F6607. Rafail Abramov is also supported by the National Science Foundation CAREER grant DMS-0845760 and the Office of Naval Research grant N00014-09-1-0083. Andrew Majda is also supported by the National Science Foundation grant DMS-0456713, the Office of Naval Research grant N00014-11-1-0306, and the Defense Advanced Research Projects Agency grant N0014-07-1-0750.

# REFERENCES


Abramov, R., 2009: Short-time linear response with reduced-rank tangent map. *Chin. Ann. Math.*, **30B (5)**, 447–462.

Abramov, R., 2010: Approximate linear response for slow variables of deterministic or stochastic dynamics with time scale separation. *J. Comput. Phys.*, **229 (20)**, 7739–7746.

Abramov, R., 2011: Improved linear response for stochastically driven systems. *Front. Math. China*, submitted.

Abramov, R. and A. Majda, 2007: Blended response algorithms for linear fluctuation-dissipation for complex nonlinear dynamical systems. *Nonlinearity*, **20**, 2793–2821.

Abramov, R. and A. Majda, 2008: New approximations and tests of linear fluctuation-response for chaotic nonlinear forced-dissipative dynamical systems. *J. Nonlin. Sci.*, **18 (3)**, 303–341.

Abramov, R. and A. Majda, 2009: New algorithms for low frequency climate response. *J. Atmos. Sci.*, **66**, 286–309.

Bell, T., 1980: Climate sensitivity from fluctuation dissipation: Some simple model tests. *J. Atmos. Sci.*, **37 (8)**, 1700–1708.

Carnevale, G., M. Falcioni, S. Isola, R. Purini, and A. Vulpiani, 1991: Fluctuation-response in systems with chaotic behavior. *Phys. Fluids A*, **3 (9)**, 2247–2254.

Deker, U. and F. Haake, 1975: Fluctuation-dissipation theorems for classical processes. *Phys. Rev. A*, **11**, 2043–2056.

Eckmann, J. and D. Ruelle, 1985: Ergodic theory of chaos and strange attractors. *Rev. Mod. Phys.*, **57 (3)**, 617–656.

Gershgorin, B. and A. Majda, 2010: A test model for fluctuation-dissipation theorems with time periodic statistics. *Physica D*, **239 (17)**, 1741–1757.

Gritsun, A., 2001: Fluctuation-dissipation theorem on attractors of atmospheric models. *Russ. J. Numer. Math. Modeling*, **16 (2)**, 115–133.

Gritsun, A. and G. Branstator, 2007: Climate response using a three-dimensional operator based on the fluctuation-dissipation theorem. *J. Atmos. Sci.*, **64**, 2558–2575.

Gritsun, A., G. Branstator, and V. Dymnikov, 2002: Construction of the linear response operator of an atmospheric general circulation model to small external forcing. *Num. Anal. Math. Modeling*, **17**, 399–416.

Gritsun, A., G. Branstator, and A. Majda, 2008: Climate response of linear and quadratic functionals using the fluctuation dissipation theorem. *J. Atmos. Sci.*, **65**, 2824–2841.

Gritsun, A. and V. Dymnikov, 1999: Barotropic atmosphere response to small external actions. theory and numerical experiments. *Atmos. Ocean Phys.*, **35 (5)**, 511–525.

Leith, C., 1975: Climate response and fluctuation-dissipation. *J. Atmos. Sci.*, **32**, 2022–2025.

Majda, A., R. Abramov, and B. Gershgorin, 2010a: High skill in low frequency climate

response through fluctuation dissipation theorems despite structural instability. *Proc. Natl. Acad. Sci.*, **107 (2)**, 581–586.

Majda, A., R. Abramov, and M. Grote, 2005: *Information Theory and Stochastics for Multiscale Nonlinear Systems*, CRM Monograph Series of Centre de Recherches Mathématiques, Université de Montréal, Vol. 25. American Mathematical Society, ISBN 0-8218-3843-1.

Majda, A., B. Gershgorin, and Y. Yuan, 2010b: Low frequency response and fluctuation-dissipation theorems: Theory and practice. *J. Atmos. Sci.*, **67**, 1186–1201.

Majda, A. and M. Hairer, 2010: A simple framework to justify linear response theory. *Nonlinearity*, **23 (4)**, 909–922.

Majda, A. and X. Wang, 2010: Linear response theory for statistical ensembles in complex systems with time-periodic forcing. *Comm. Math. Sci.*, **8 (1)**, 145–172.

McCalpin, J., 1995: The statistics and sensitivity of a double-gyre model: The reduced gravity, quasigeostrophic case. *J. Phys. Oceanogr.*, **25**, 806–824.

McCalpin, J. and D. Haidvogel, 1996: Phenomenology of the low-frequency variability in a reduced-gravity, quasigeostrophic double-gyre model. *J. Phys. Oceanogr.*, **26**, 739–752.

Risken, F., 1988: *The Fokker-Planck Equation*. 2d ed., Springer-Verlag, New York.

Ruelle, D., 1997: Differentiation of SRB states. *Comm. Math. Phys.*, **187**, 227–241.

Ruelle, D., 1998: General linear response formula in statistical mechanics, and the fluctuation-dissipation theorem far from equilibrium. *Phys. Lett. A*, **245**, 220–224.

Young, L.-S., 2002: What are SRB measures, and which dynamical systems have them? *J. Stat. Phys.*, **108 (5-6)**, 733–754.

# List of Tables

TABLE 1. Physical parameters of the model

| Parameter | Value |
|---|---|
| $r$ | $10^{-7}\,s^{-1}$ |
| $A_b$ | $8 \cdot 10^{10}\,m^4\,s^{-1}$ |
| $f_0$ | $7.27 \cdot 10^{-5}\,s^{-1}$ |
| $\beta$ | $1.98 \cdot 10^{-11}\,m^{-1}\,s^{-1}$ |
| $\gamma^2 = \dfrac{f_0^2}{g'H}$ | $\dfrac{1}{47636^2}\,m^{-2}$ |
| $g' = g\dfrac{\Delta\rho}{\rho_0}$ | $0.02\,m\,s^{-2}$ |
| $\rho_0$ | $1027\,kg\,m^{-3}$ |
| $\tau_0$ | $0.05\,N\,m^{-2}$ |
| $\alpha$ | $0.05$ |

# List of Figures

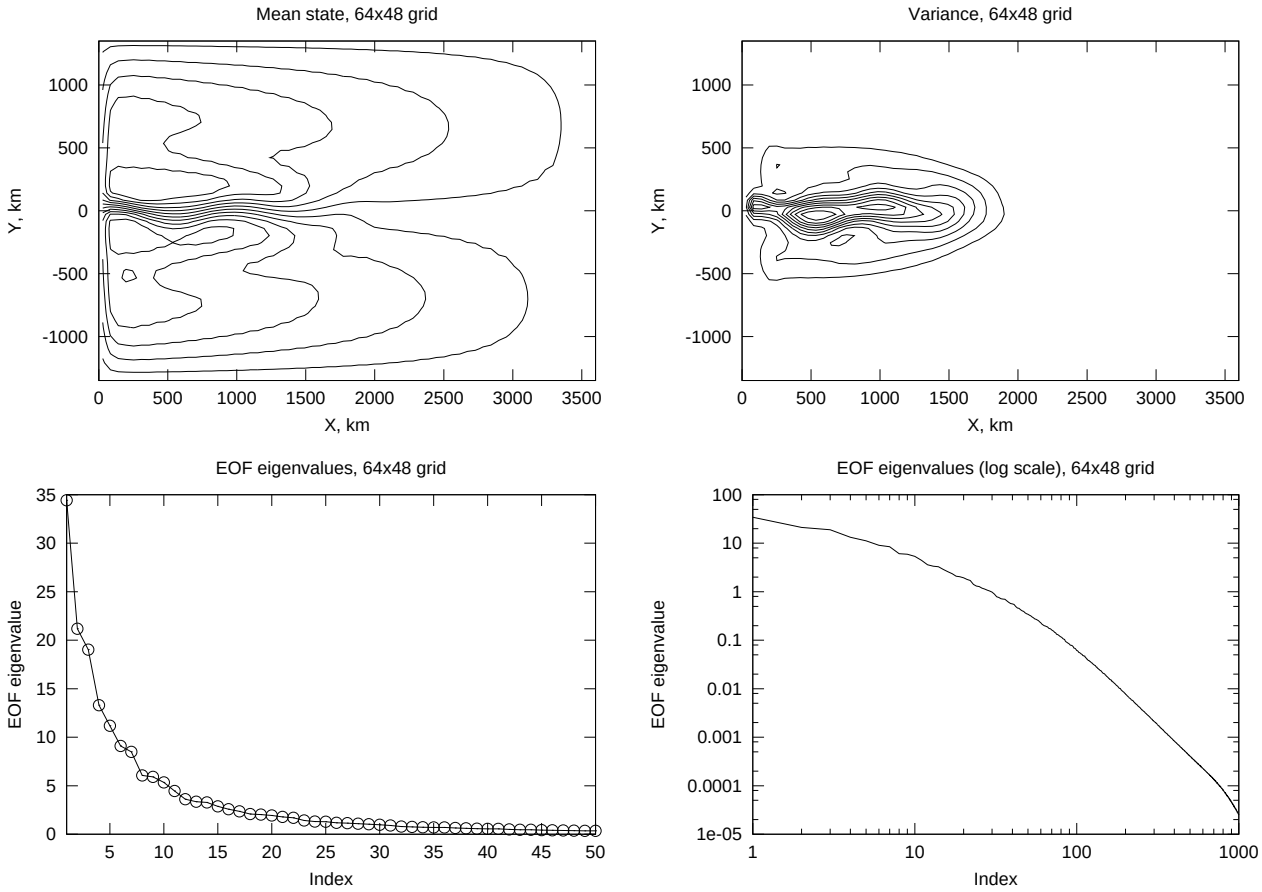


FIG. 1. Top row: the mean state and variance of the model, interface anomaly. Bottom row: EOF eigenvalues.

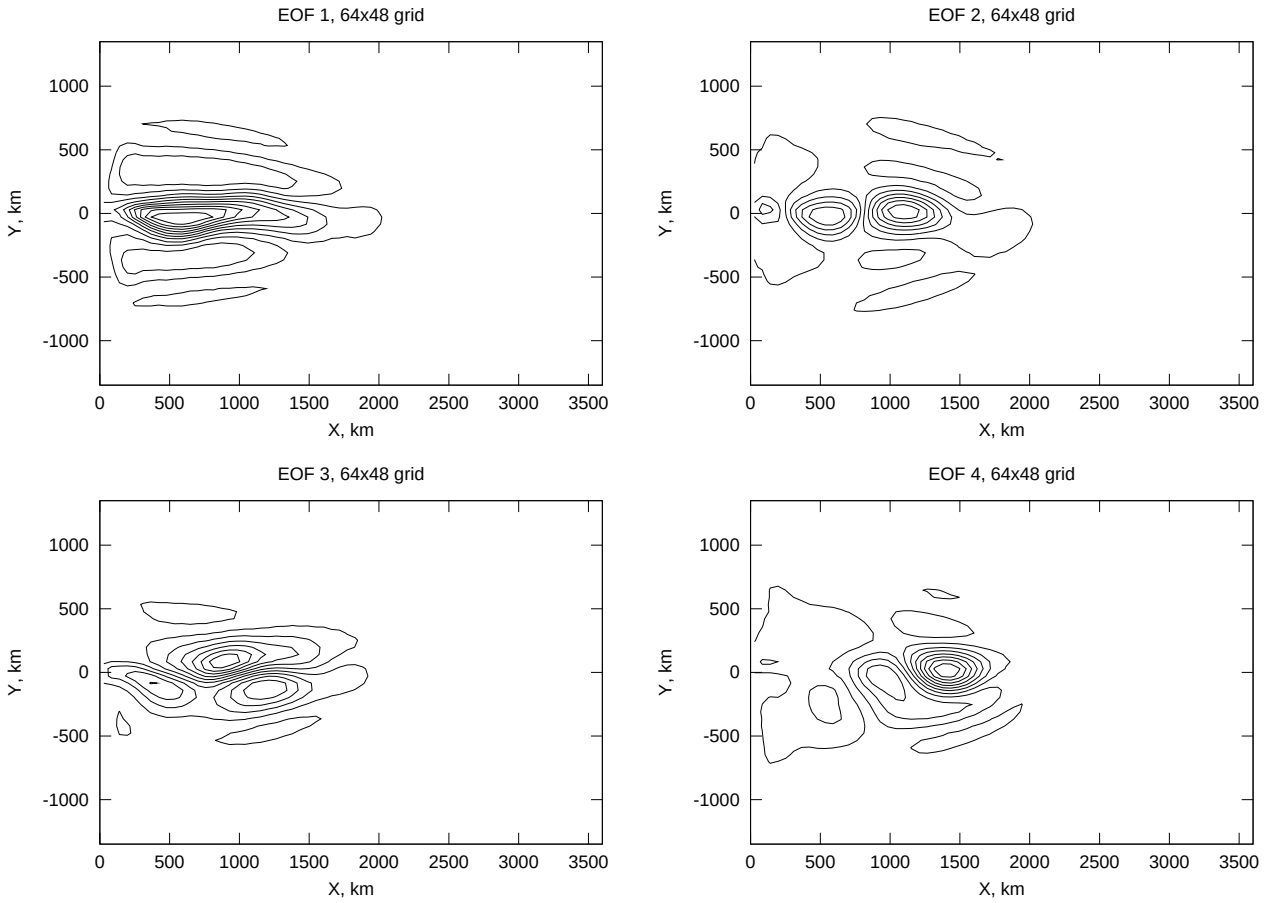
EOF 1, 64x48 grid
EOF 2, 64x48 grid
EOF 3, 64x48 grid
EOF 4, 64x48 grid
Y, km
X, km
1000
500
0
-500
-1000
0
500
1000
1500
2000
2500
3000
3500

FIG. 2. EOFs 1–4.

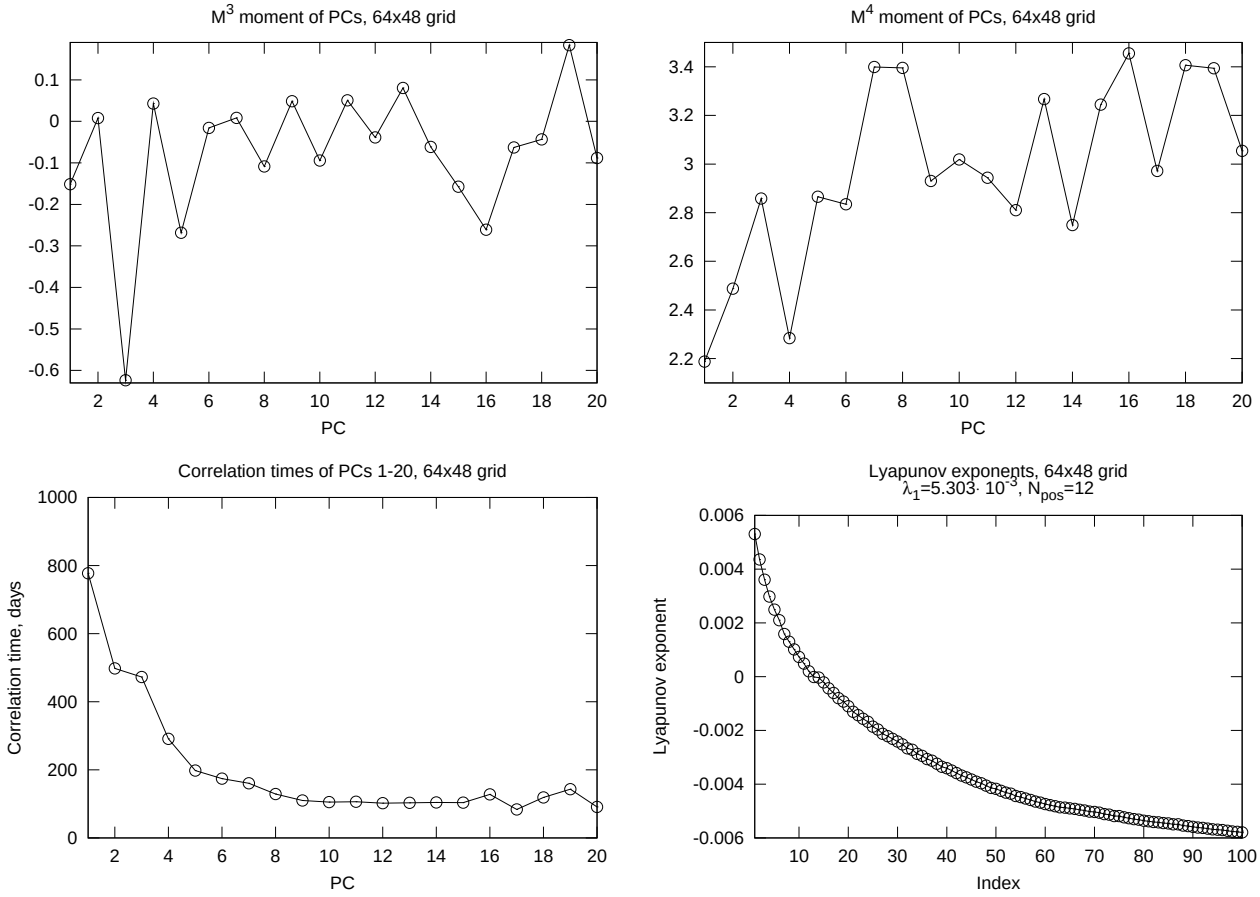


FIG. 3. Top row: skewness and flatness of the first 20 PCs. Bottom left – autocorrelation times, bottom right – Lyapunov exponents.

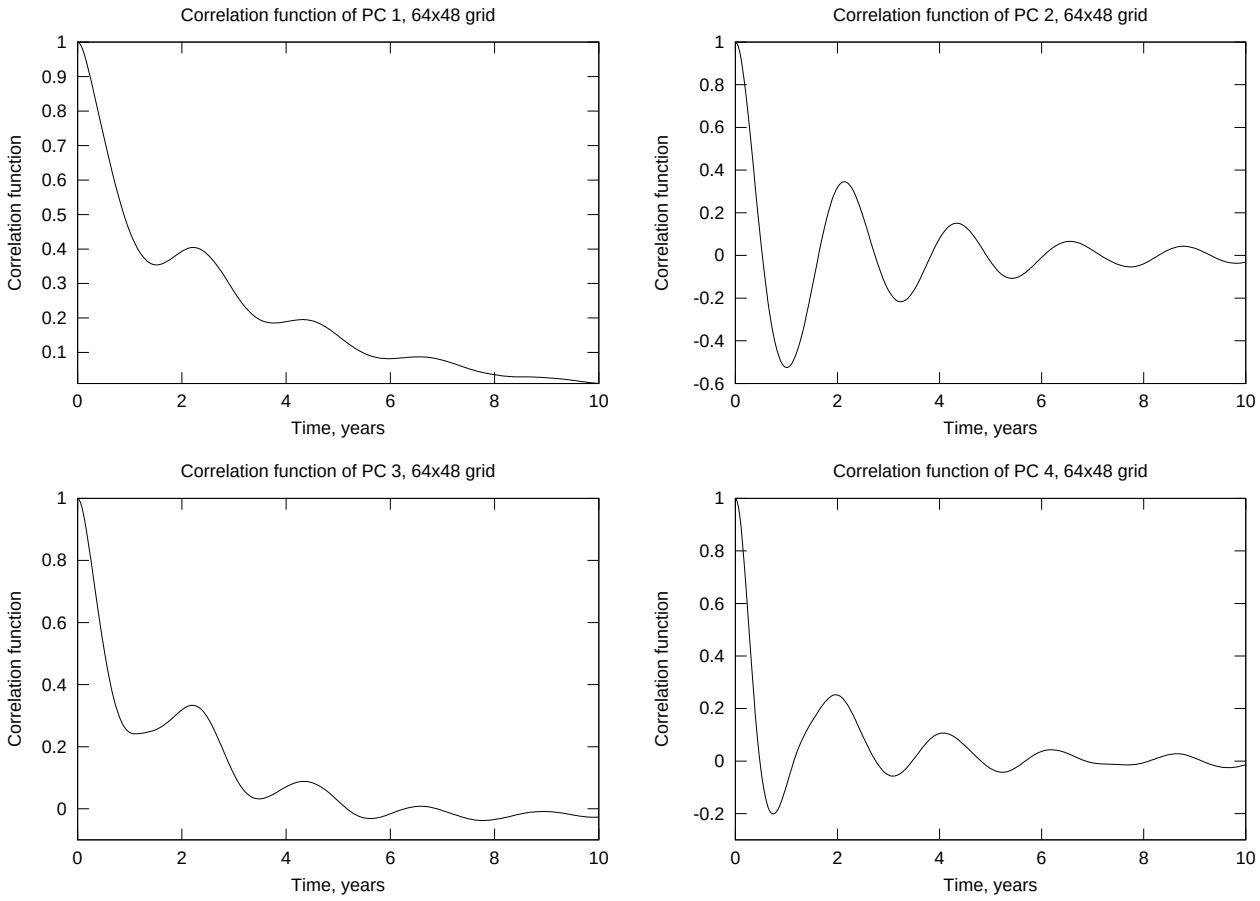


FIG. 4. Correlation functions of the PCs 1–4.

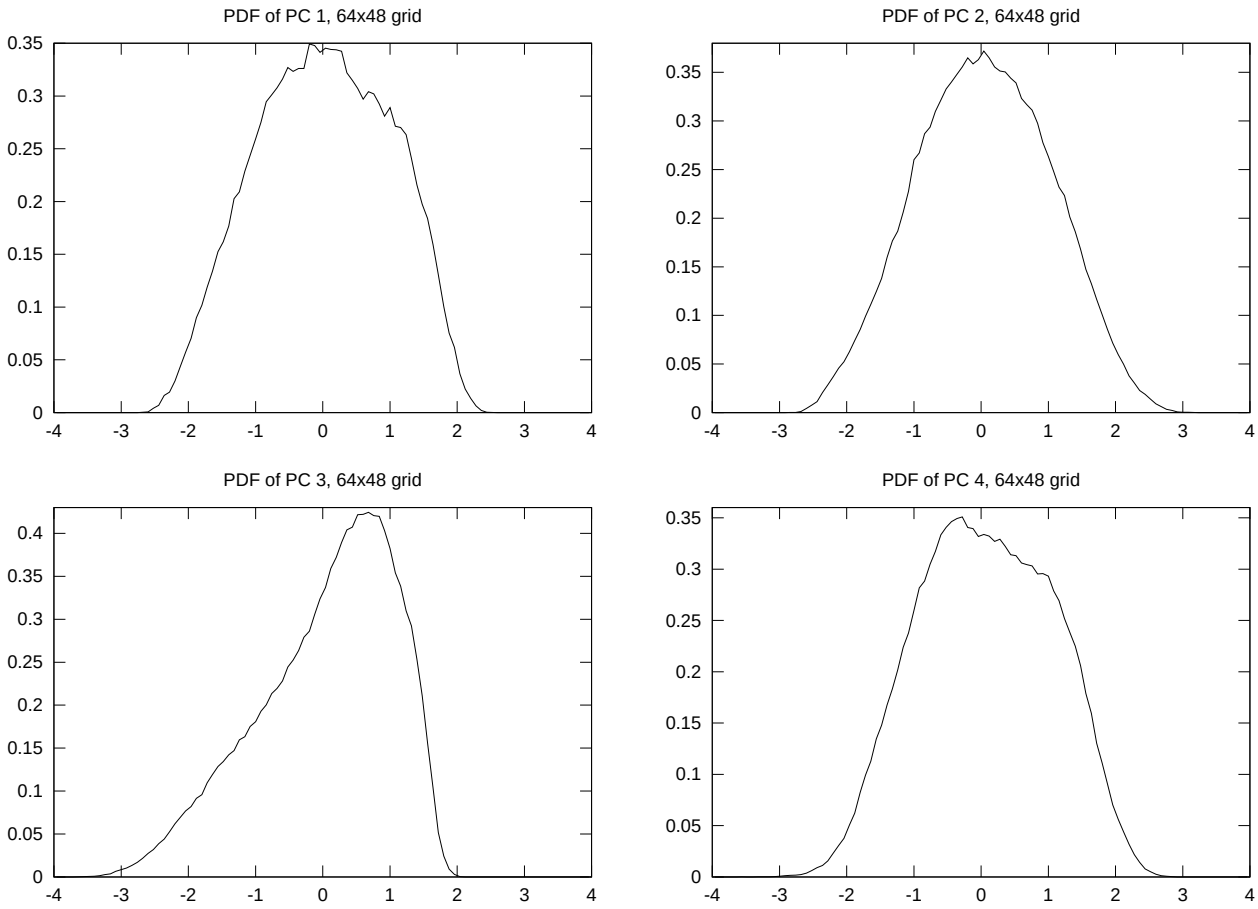


FIG. 5. Probability density functions of the PCs 1–4.

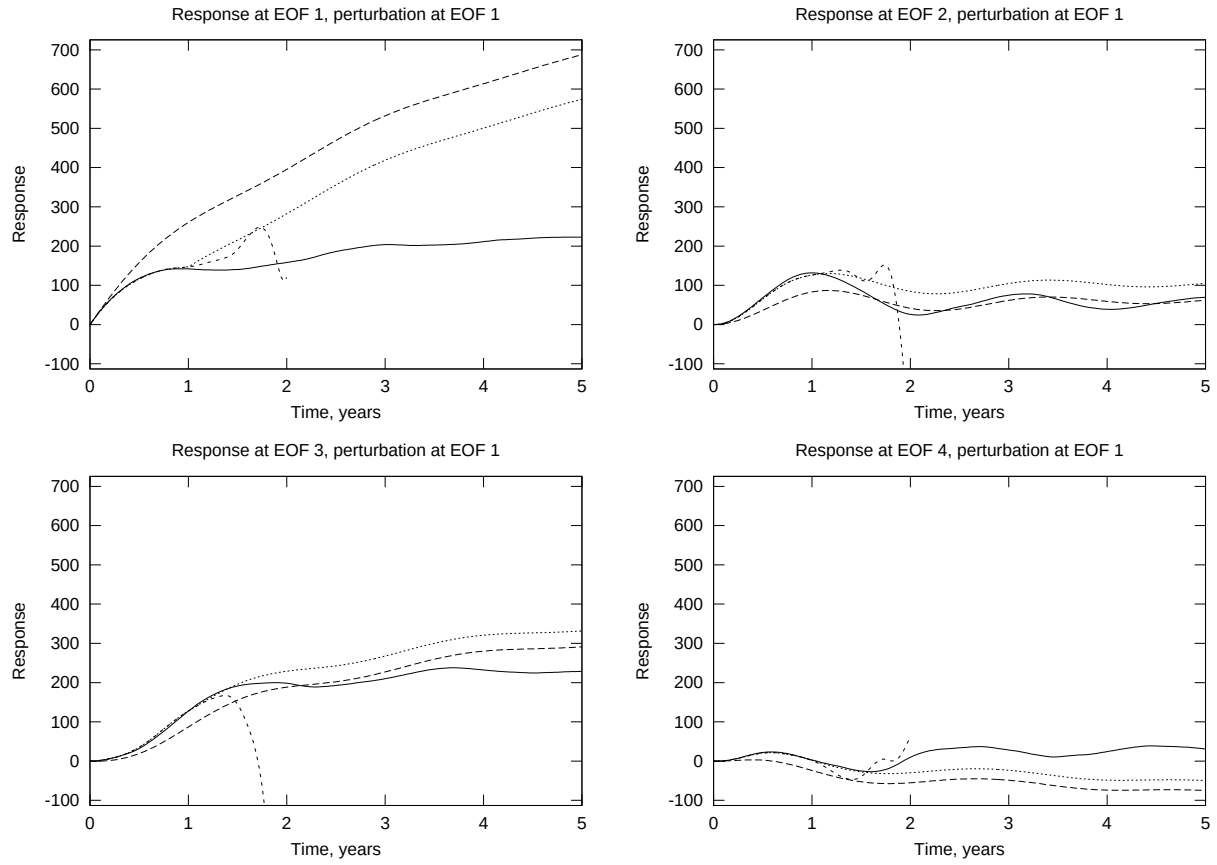


FIG. 6. Mean response at EOFs 1–4, perturbation at EOF 1, tangent map rank for ST-FDT is 1536. Solid line – ideal response, long-dashed line – qG-FDT response, short-dashed line – ST-FDT response, dotted line – ST/qG-FDT response.

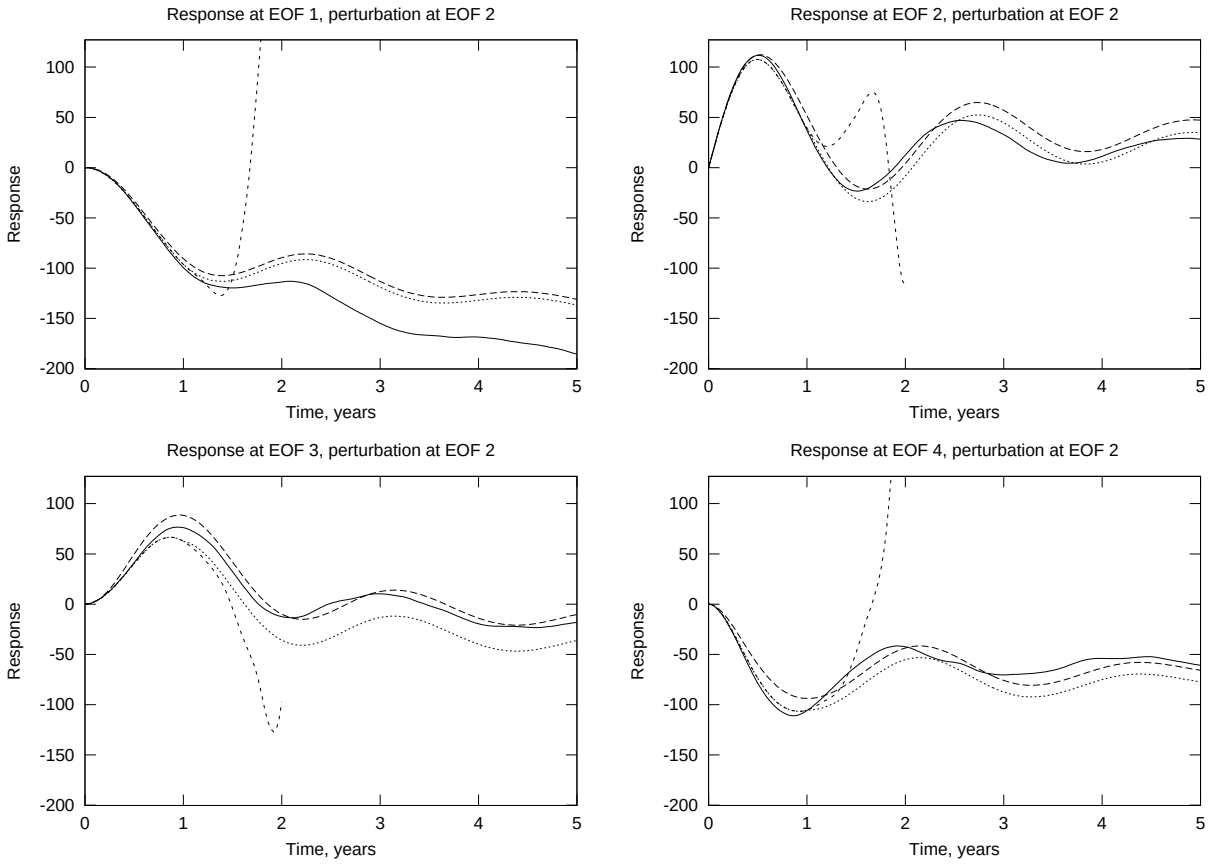


FIG. 7. Mean response at EOFs 1–4, perturbation at EOF 2, tangent map rank for ST-FDT is 1536. Solid line – ideal response, long-dashed line – qG-FDT response, short-dashed line – ST-FDT response, dotted line – ST/qG-FDT response.

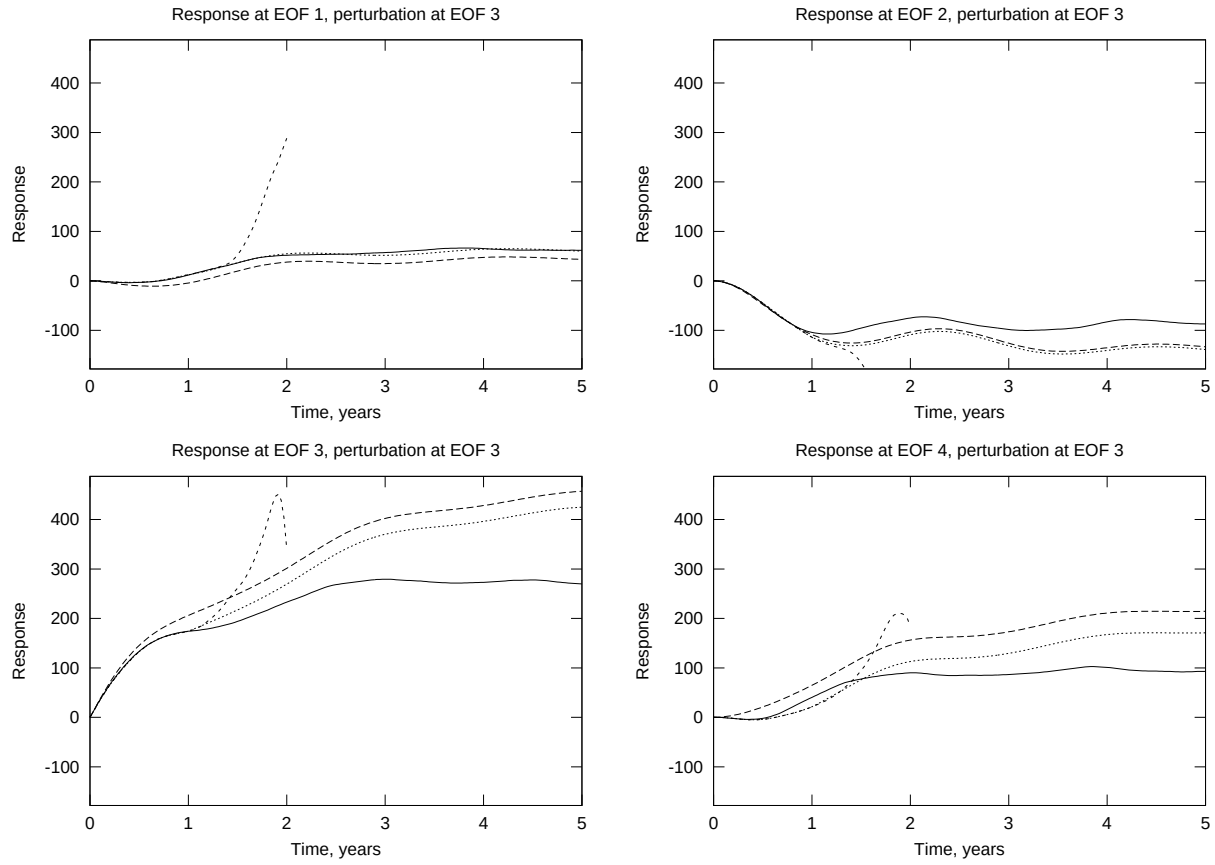


FIG. 8. Mean response at EOFs 1–4, perturbation at EOF 3, tangent map rank for ST-FDT is 1536. Solid line – ideal response, long-dashed line – qG-FDT response, short-dashed line – ST-FDT response, dotted line – ST/qG-FDT response.

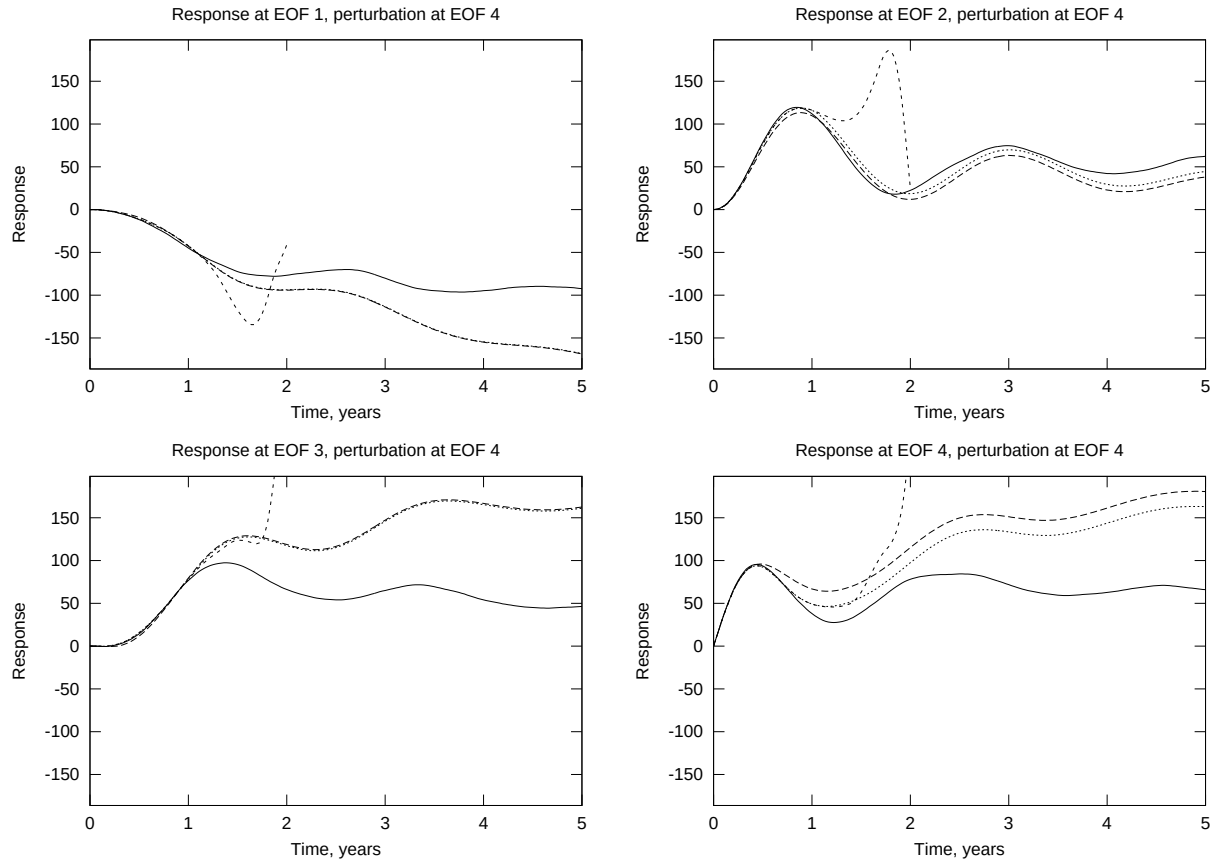


FIG. 9. Mean response at EOFs 1–4, perturbation at EOF 4, tangent map rank for ST-FDT is 1536. Solid line – ideal response, long-dashed line – qG-FDT response, short-dashed line – ST-FDT response, dotted line – ST/qG-FDT response.

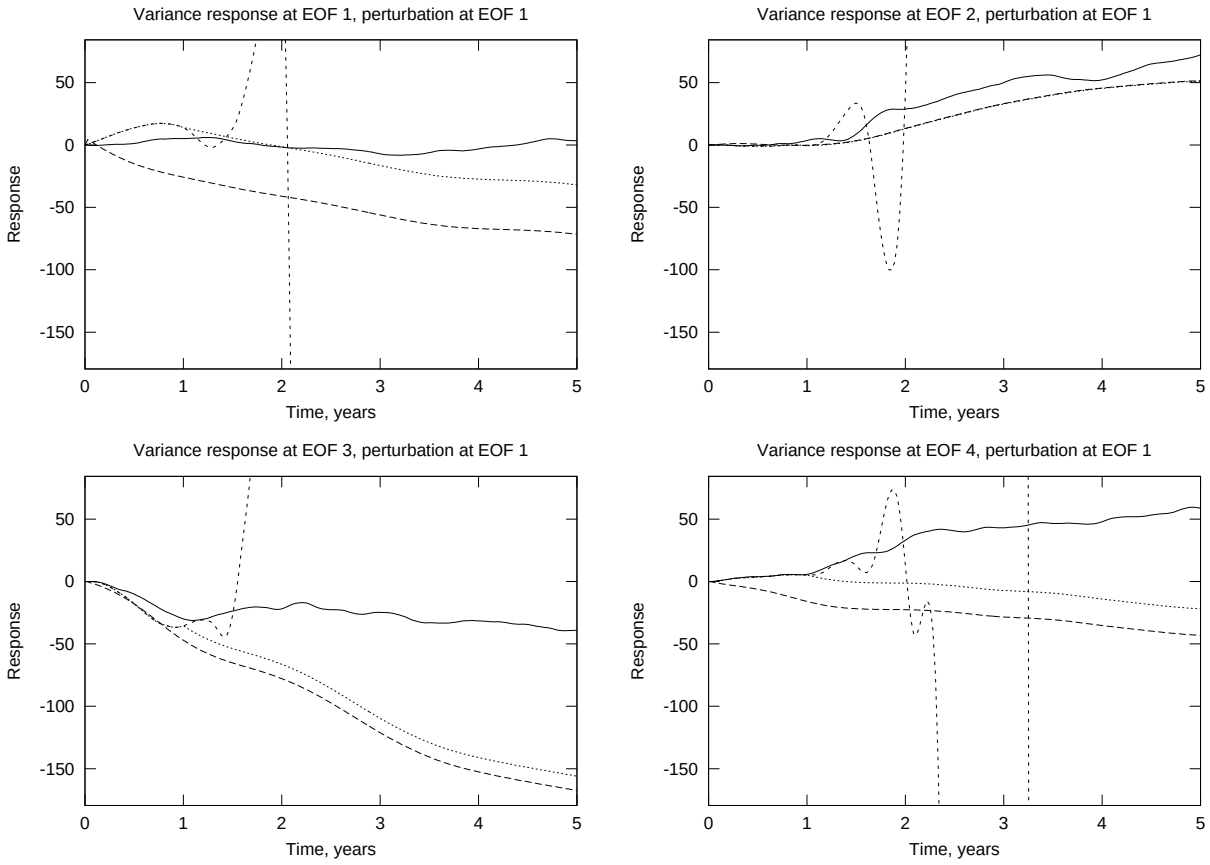


FIG. 10. Variance response at EOFs 1–4, perturbation at EOF 1, tangent map rank for ST-FDT is 1536. Solid line – ideal response, long-dashed line – qG-FDT response, short-dashed line – ST-FDT response, dotted line – ST/qG-FDT response.

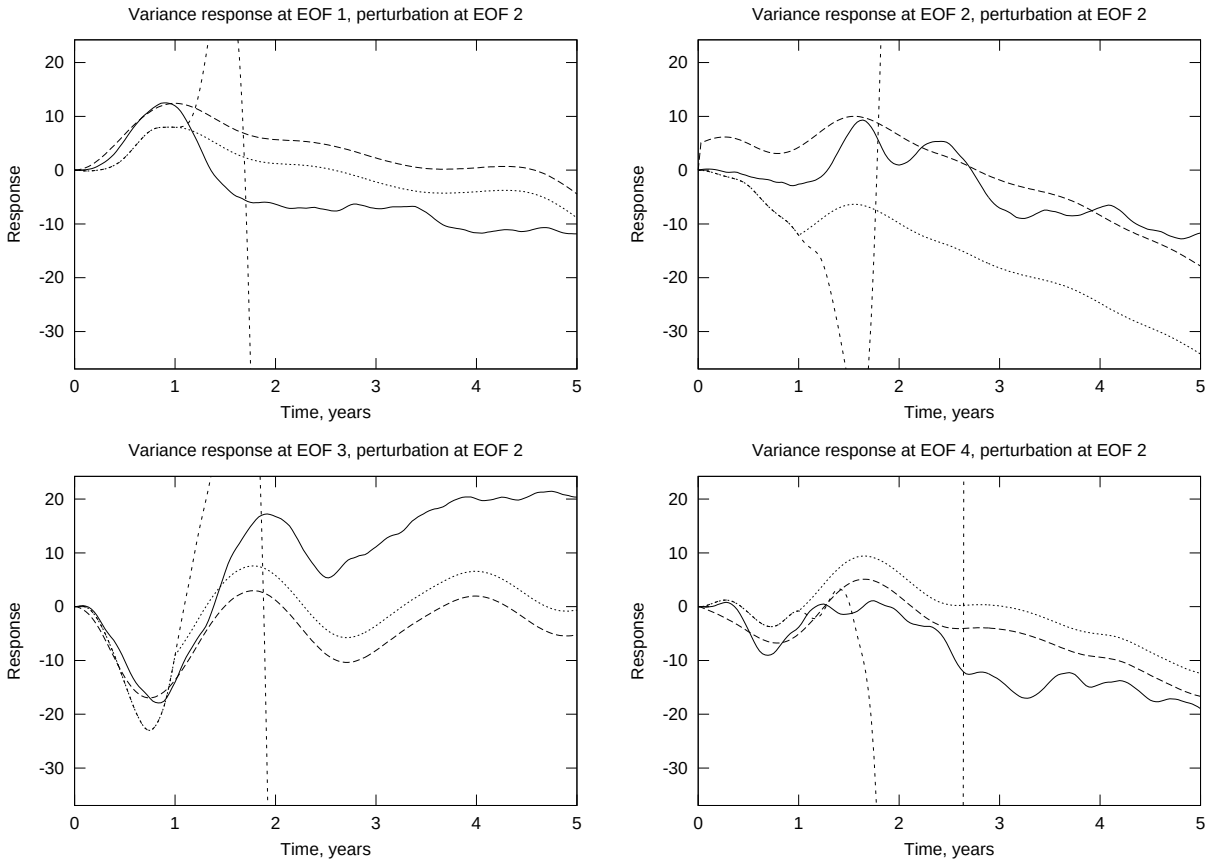


FIG. 11. Variance response at EOFs 1–4, perturbation at EOF 2, tangent map rank for ST-FDT is 1536. Solid line – ideal response, long-dashed line – qG-FDT response, short-dashed line – ST-FDT response, dotted line – ST/qG-FDT response.

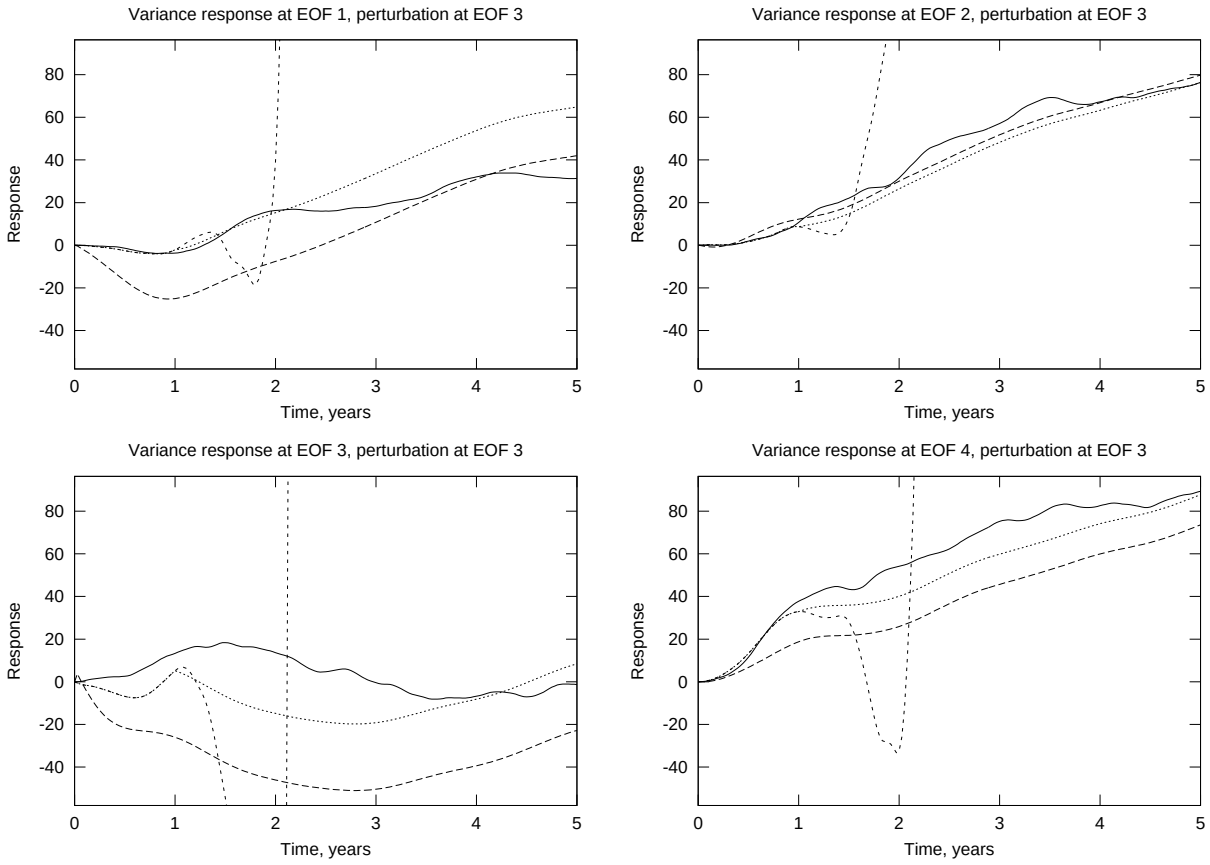


FIG. 12. Variance response at EOFs 1–4, perturbation at EOF 3, tangent map rank for ST-FDT is 1536. Solid line – ideal response, long-dashed line – qG-FDT response, short-dashed line – ST-FDT response, dotted line – ST/qG-FDT response.

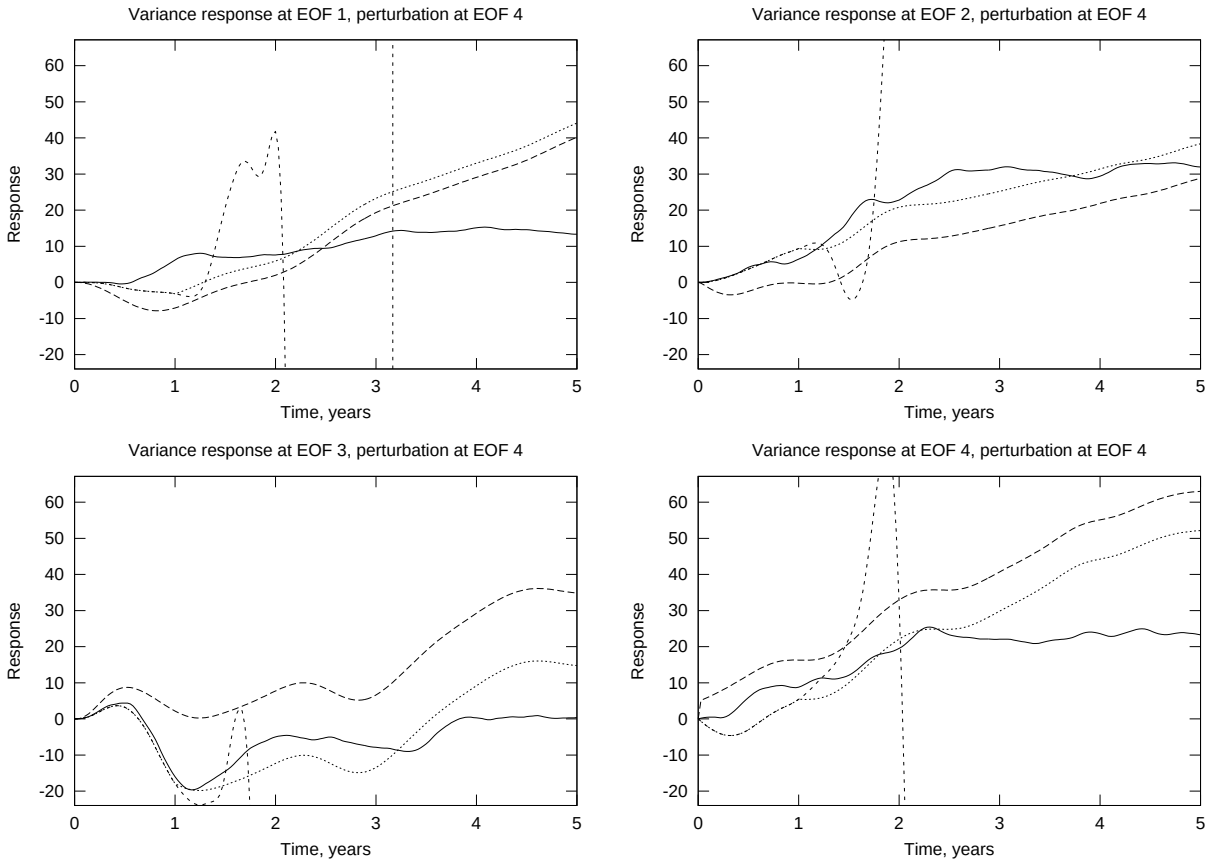


FIG. 13. Variance response at EOFs 1–4, perturbation at EOF 4, tangent map rank for ST-FDT is 1536. Solid line – ideal response, long-dashed line – qG-FDT response, short-dashed line – ST-FDT response, dotted line – ST/qG-FDT response.

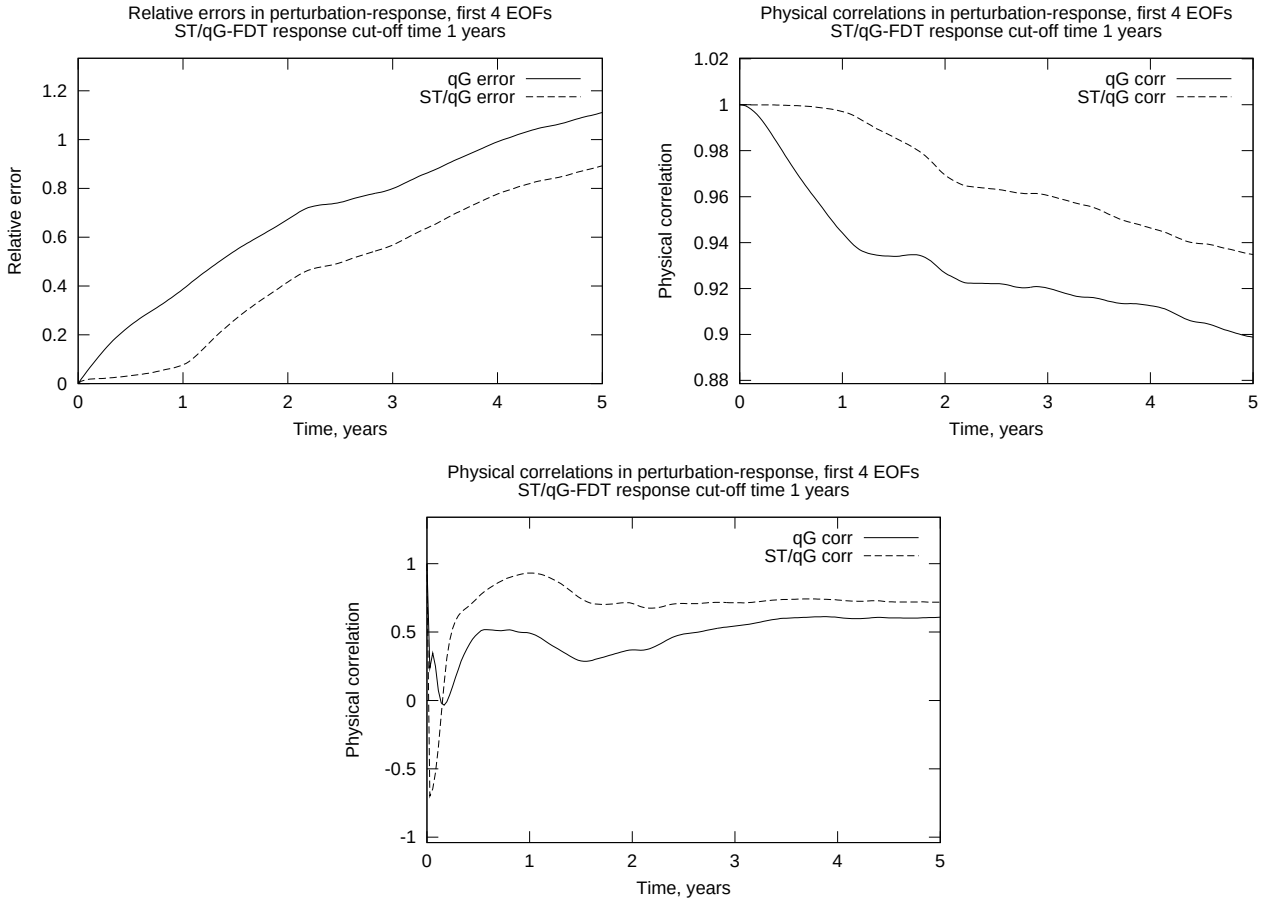


FIG. 14. Top row: relative errors and physical correlations between the mean state ideal response and qG-FDT, ST/qG-FDT responses for the first 4 EOFs. Bottom: physical correlations between the variance ideal response and qG-FDT, ST/qG-FDT responses for the first 4 EOFs. The tangent map rank for ST/qG-FDT is 1536, cut-off time 1 year.

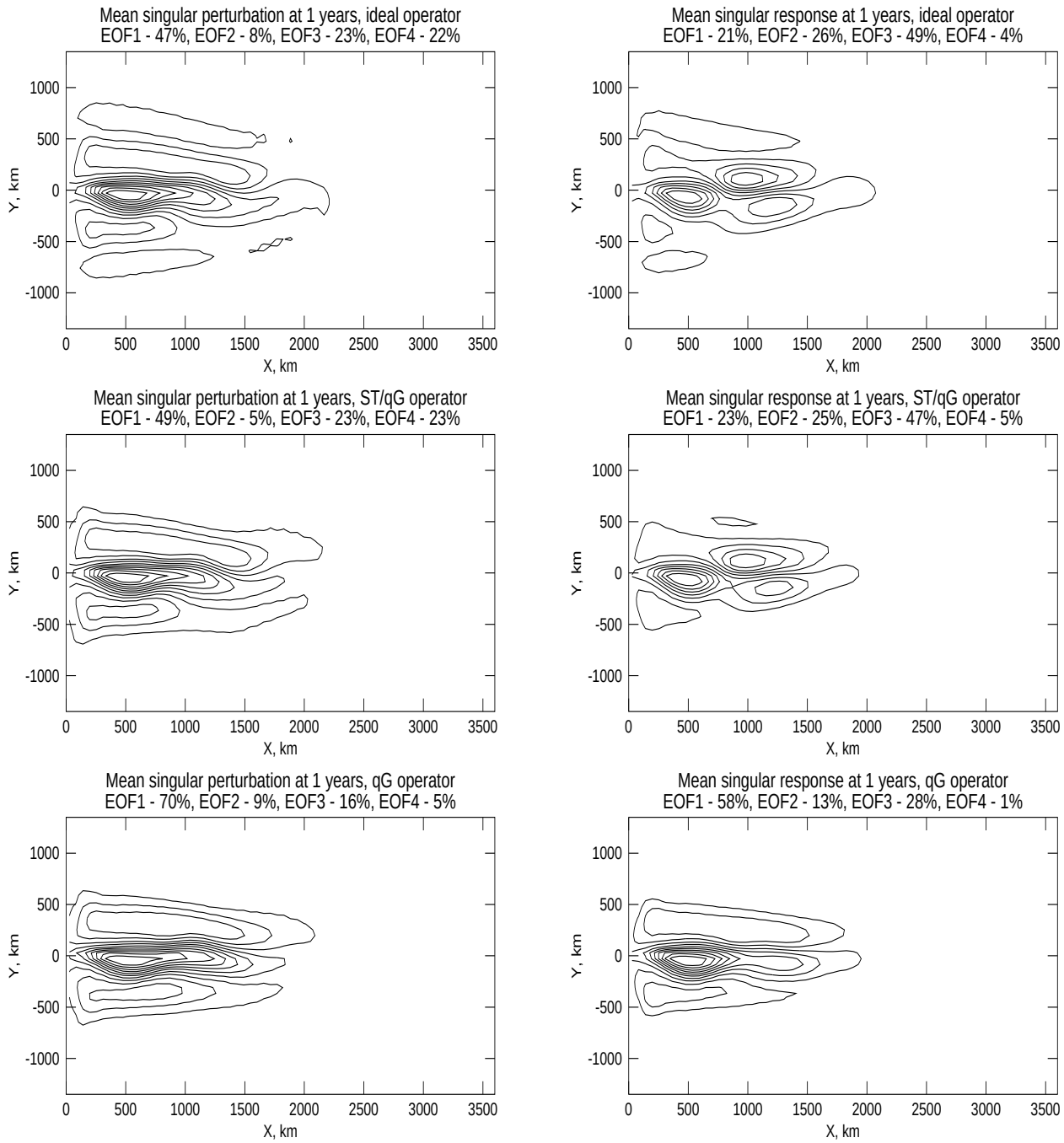


FIG. 15. The perturbation and response corresponding to the largest singular value of the mean state response operator at 1 year response time. The tangent map rank for ST/qG-FDT is 1536, cut-off time 1 year.

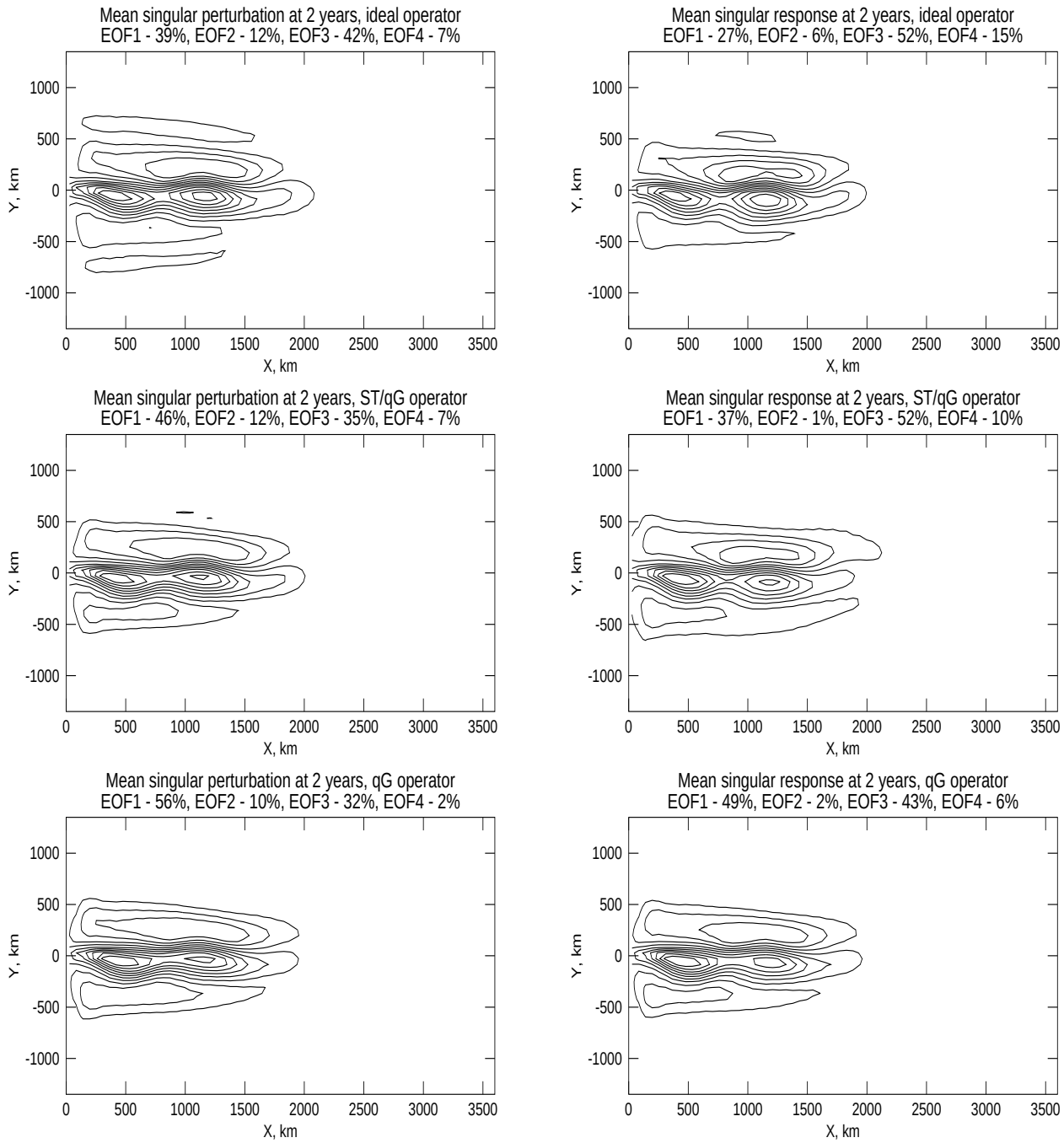


FIG. 16. The perturbation and response corresponding to the largest singular value of the mean state response operator at 2 year response time. The tangent map rank for ST/qG-FDT is 1536, cut-off time 1 year.

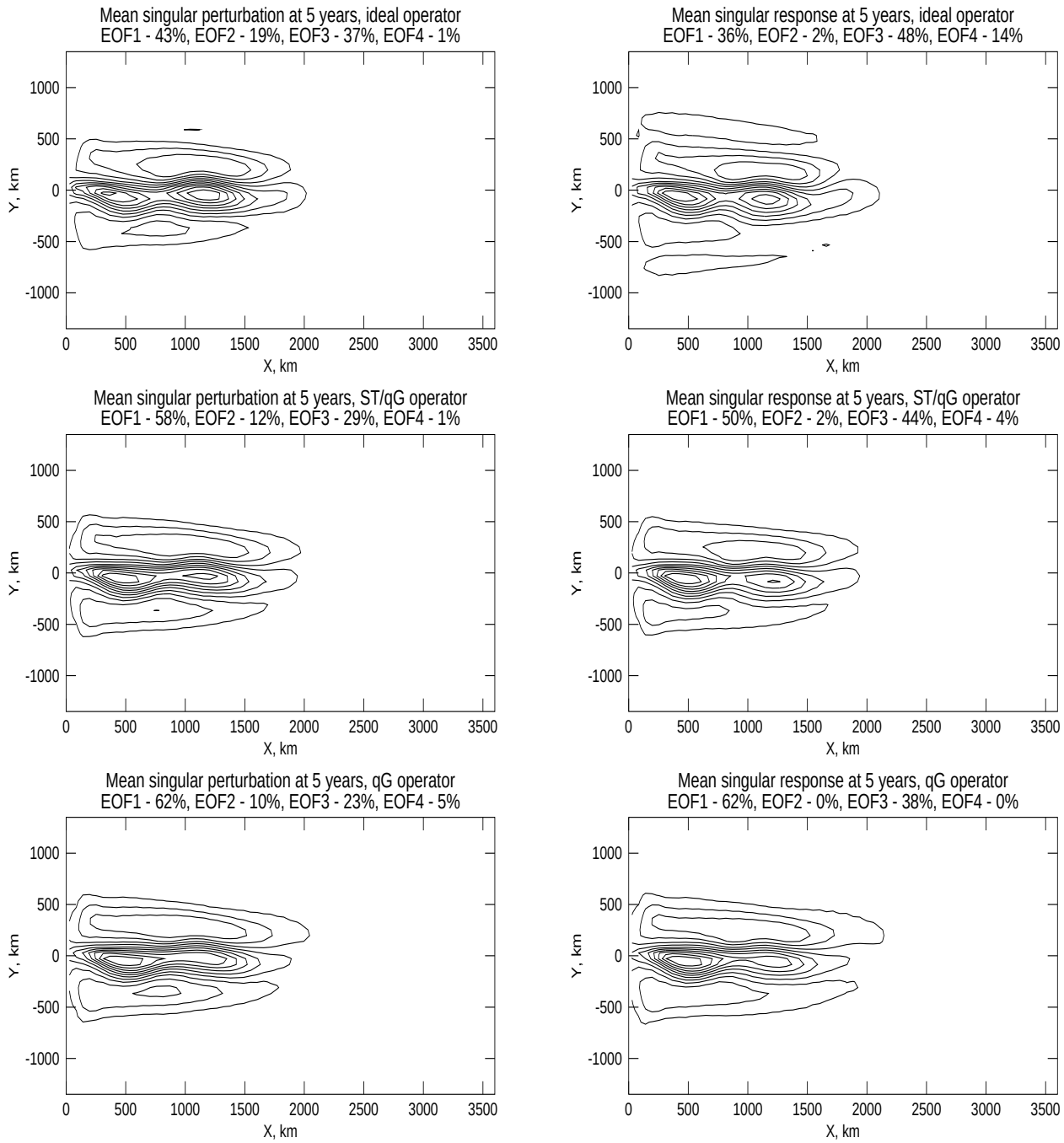


FIG. 17. The perturbation and response corresponding to the largest singular value of the mean state response operator at 5 year response time. The tangent map rank for ST/qG-FDT is 1536, cut-off time 1 year.

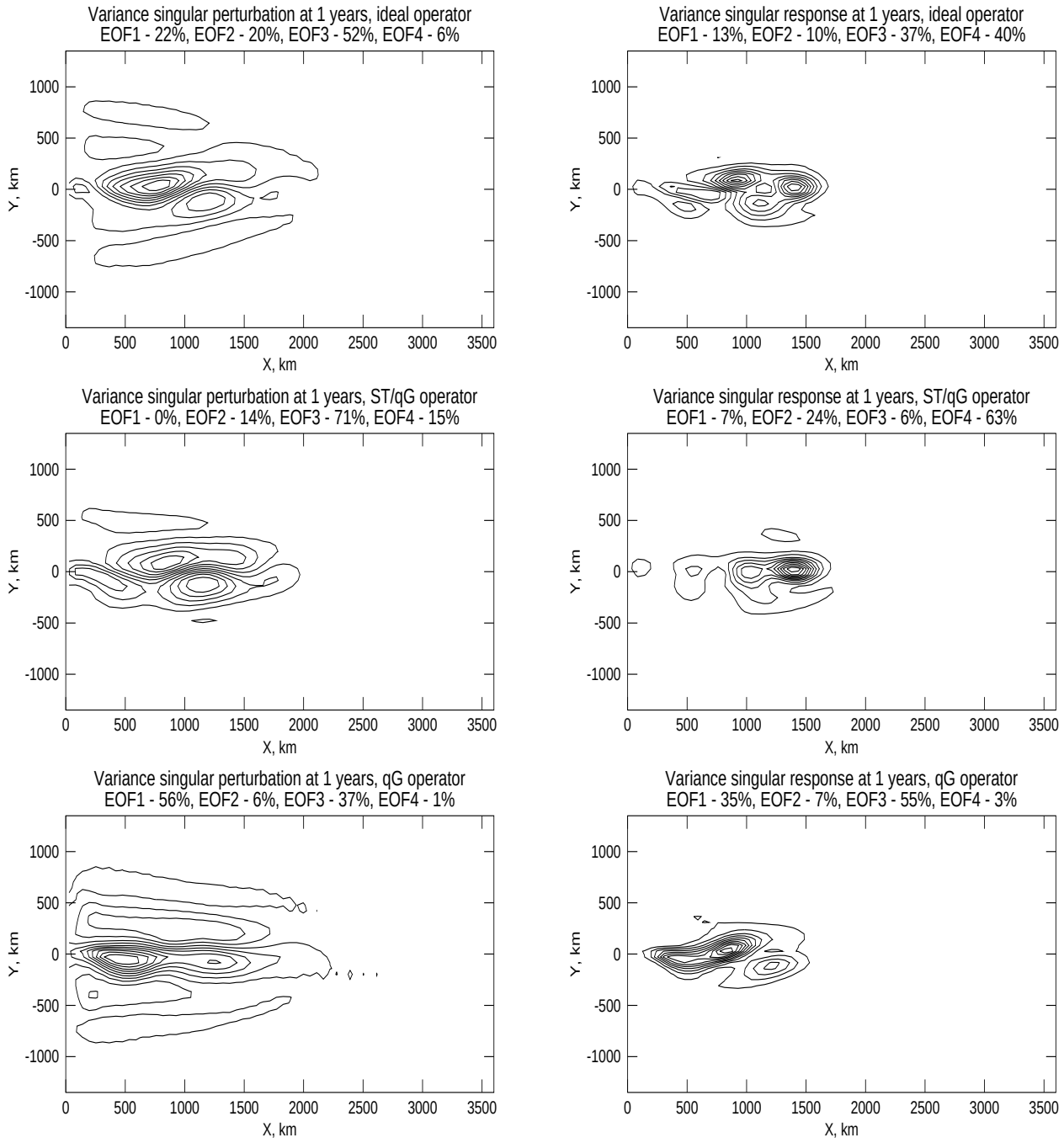


FIG. 18. The perturbation and response corresponding to the largest singular value of the variance response operator at 1 year response time. The tangent map rank for ST/qG-FDT is 1536, cut-off time 1 year.

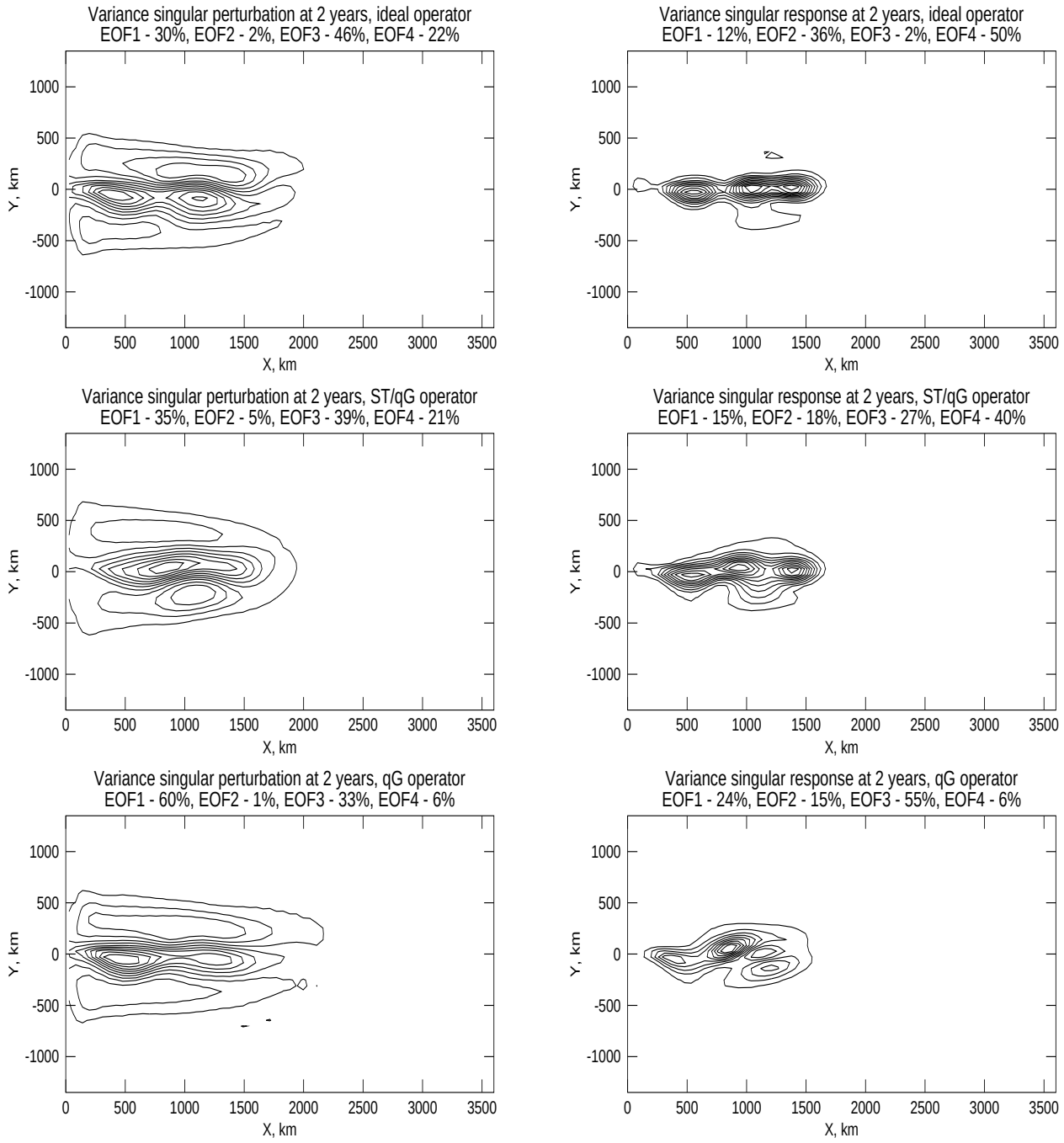


FIG. 19. The perturbation and response corresponding to the largest singular value of the variance response operator at 2 year response time. The tangent map rank for ST/qG-FDT is 1536, cut-off time 1 year.

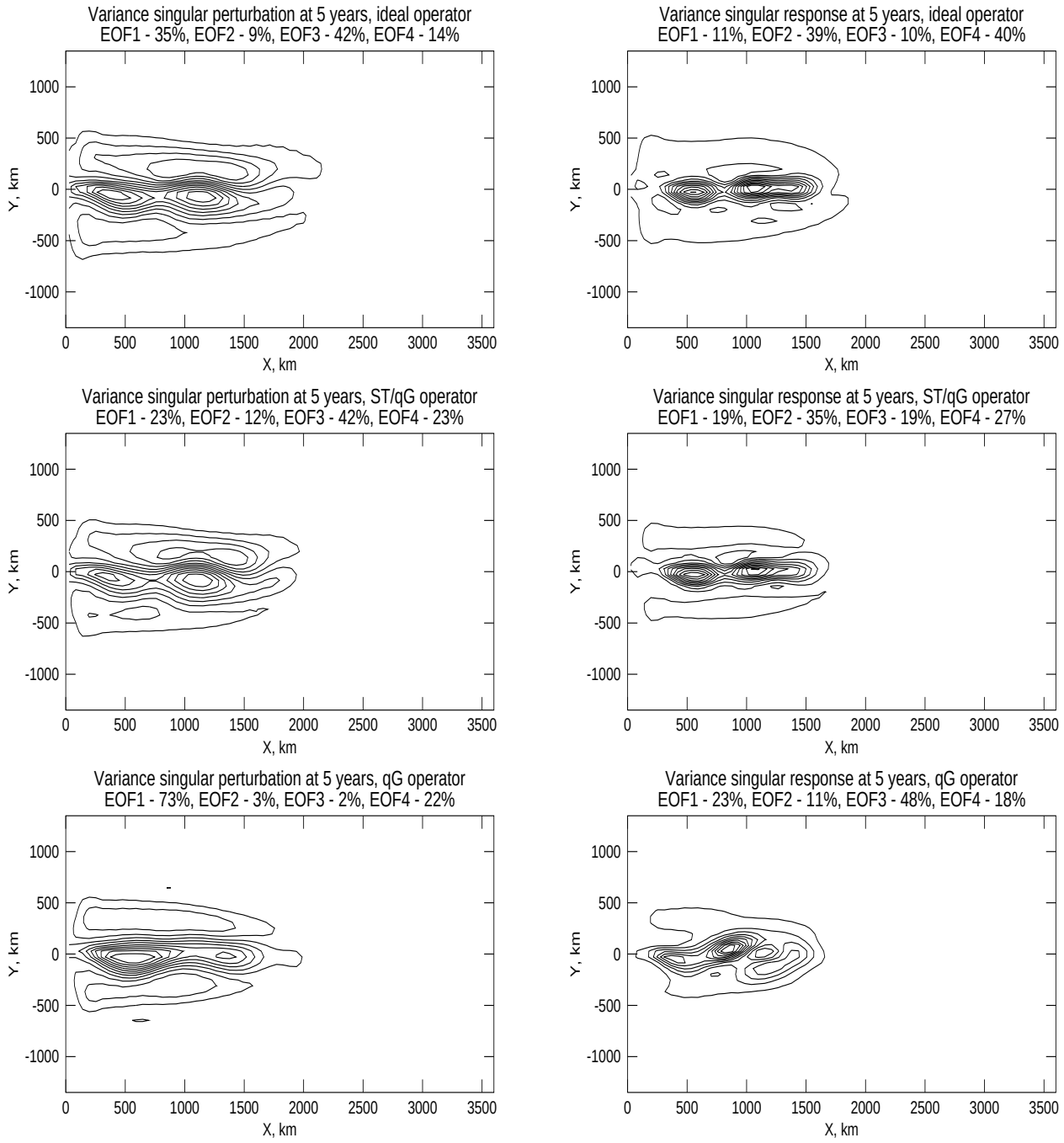


FIG. 20. The perturbation and response corresponding to the largest singular value of the variance response operator at 5 year response time. The tangent map rank for ST/qG-FDT is 1536, cut-off time 1 year.